Supplementary Information

Engineering Intraporous Solvent Environments: Effects of Aqueous-Organic Solvent Mixtures on Competition Between Zeolite-Catalyzed Epoxidation and H_2O_2 Decomposition Pathways

David S. Potts, Chris Torres, Ohsung Kwon, David W. Flaherty

Department of Chemical and Biomolecular Engineering
University of Illinois Urbana-Champaign, Urbana, Illinois 61801 (USA)

*Corresponding author e-mail: dwflhrty@illinois.edu

S1. Catalyst Characterization

S1.1 Diffuse Reflectance UV-Vis Spectra to Infer Ti Atom Dispersity
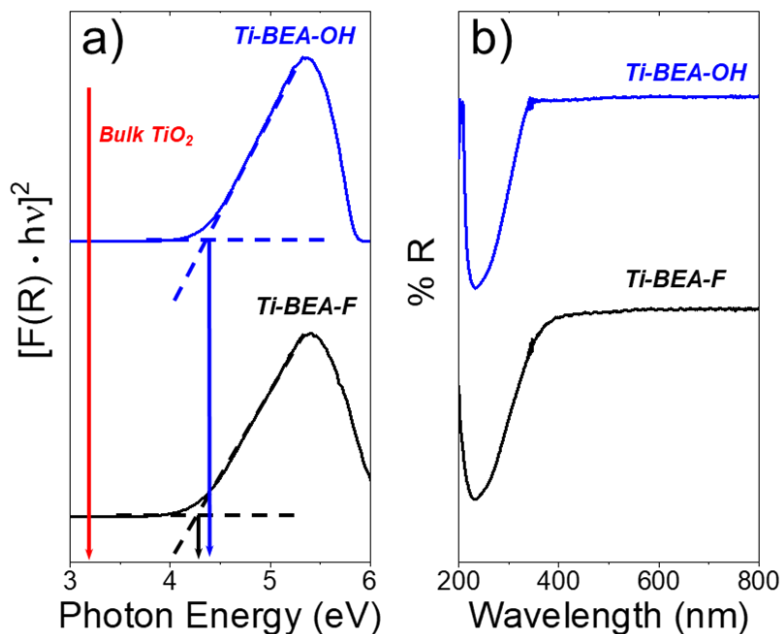

Figure S1. a) Tauc plots and b) DR-UV-Vis spectra obtained with a UV-Vis spectrophotometer at ambient conditions for Ti-BEA-OH (blue) and Ti-BEA-F (black). Spectra were normalized to the most intense feature around 5.5 eV and 225 nm and are vertically offset for clarity.

The band gaps for each Ti-BEA (see Table 1 in the main text) were obtained by extrapolating the linear absorbance region of the Tauc plot in Figure S1a to the baseline. The intersection of the baseline and linear region represents the band gap photon energy. The band gaps for both Ti-BEA are much greater than the band gap for bulk titania (TiO_2, 3.2 eV),[1] suggesting that the titanium atoms are well dispersed within the *BEA framework.

The photon energy was obtained from the wavelength as follows:

$$Photon\ Energy\ (eV) = \frac{3 * 10^8 \frac{m}{s}}{Wavelength\ (nm) * \frac{1\ m}{10^9\ nm}} * h * \left(6.242 * 10^{18} \frac{eV}{J}\right)$$

where h equals the Planck constant. The ordinate from Figure S1a was obtained from the ordinate of the raw spectra in Figure S1b. The Kubelka-Munk function was calculated from % R:

$$F(R) = \frac{\left(1 - \frac{\%R}{100}\right)^2}{2 * \left(\frac{\%R}{100}\right)}$$

F(R) was then multiplied by the photon energy, and the resulting quantity was squared to yield the ordinate for Figure S1a.

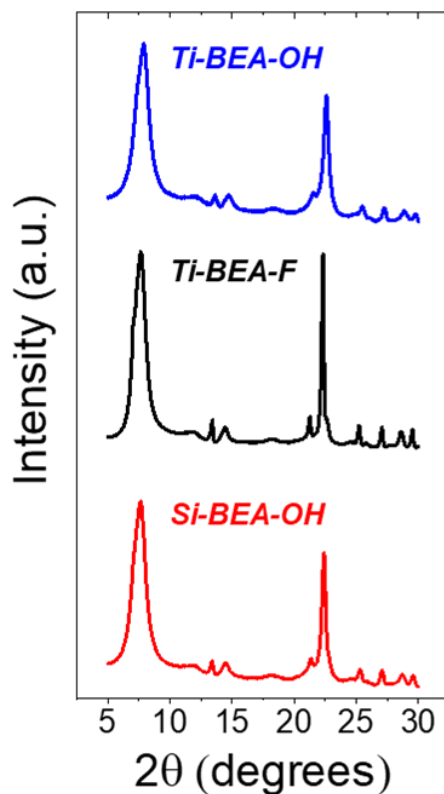## S1.2 X-Ray Diffraction to Observe Crystallinity of Ti-BEA Catalysts

Figure S2. Powder X-ray diffractograms obtained with Cu Kα radiation (0.15418 nm) under ambient conditions for Ti-BEA-OH (blue), Ti-BEA-F (black), and Si-BEA-OH (red). Spectra are vertically offset for clarity.

The crystallographic features for each Ti-BEA are representative of the *BEA framework. The sharper feature at ~22.5 degrees for Ti-BEA-F indicates a highly crystalline material, as expected for zeolites synthesized in fluoride media.[2] The broader feature for Ti-BEA-OH suggests a smaller crystallite size[3] and the presence of internal $(SiOH)_x$ defects formed by dealumination of Al-BEA-OH (Si:Al = 20).

Notably, each Ti-BEA shows a weak feature at 25.5 degrees, whereas anatase TiO_2 shows a strong feature.[4] However, the XRD pattern for dealuminated *BEA (Si-BEA-OH, initial Si:Al = 20) also contains a weak feature in this region, suggesting that the feature is characteristic of the *BEA framework. The XRD patterns in Figure S2 indicate that each Ti-BEA possesses the crystalline *BEA framework, with minimal to no TiO_2 present.

S1.3 *Ex situ* Raman Spectra of Ti-BEA Materials to Confirm Ti Coordination
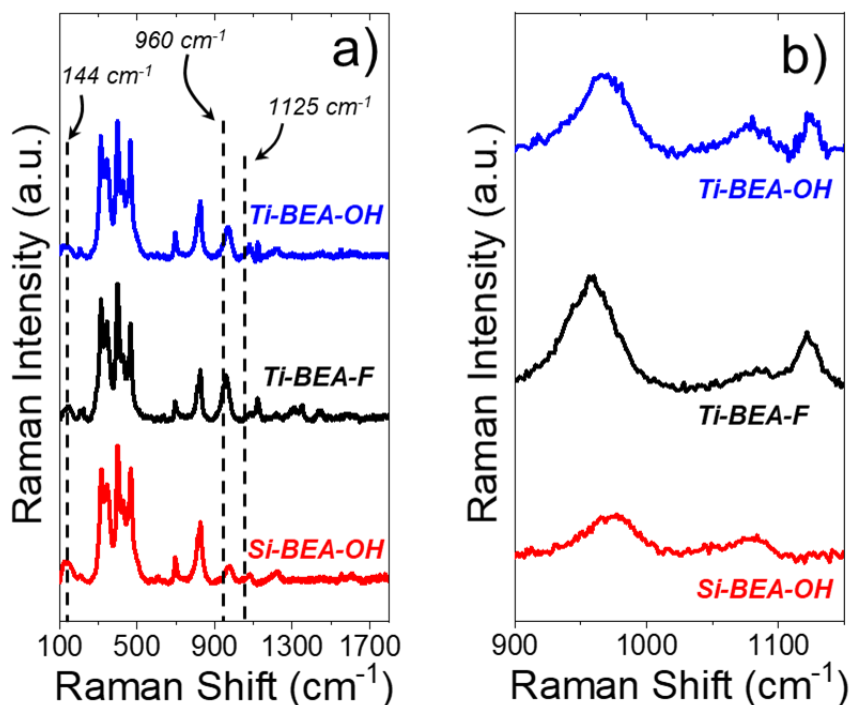

Figure S3. a) *Ex situ* Raman spectra of Ti-BEA-OH (blue), Ti-BEA-F (black), and Si-BEA-OH (red), and b) the *ex situ* spectra zoomed into the 900-1150 cm^{-1} region. The spectra are an average of 10 scans with an exposure time of 20 s. Spectra are normalized by the maximum feature at ~400 cm^{-1} and are vertically offset for clarity. The spectra were taken at ambient conditions with a Raman spectrometer (Renishaw, InVia) equipped with a 532 nm laser that delivered a power density of ~2 mW μm^{-2}.

Bulk anatase TiO_2 shows an intense E_g vibration peak at 144 cm^{-1},[5-6] which is hardly observable in the Raman spectra of each Ti-BEA. The area of this feature is also slightly more intense in Si-BEA-OH, which suggests the feature results from a mode inherent to the *BEA framework instead of TiO_2. The intense peaks between 250 and 550 cm^{-1} represent features of the *BEA framework: the peaks at 315 and 345 cm^{-1} are assigned to six-membered rings, the peaks at 400 and 425 cm^{-1} are assigned to five-membered rings, and the peak at 465 cm^{-1} represents four-membered rings characteristic of the *BEA framework.[7-8] The peak at ~695 cm^{-1} has previously been reported on Raman spectra of crystalline *BEA zeolites, suggesting the feature may be characteristic of the *BEA framework.[9-10] The peak at ~820 cm^{-1} represents a symmetric skeletal mode of microporous silicates.[11-12]

The feature at ~960 cm^{-1} has been commonly attributed to silanol defects[13-15] and Ti atoms incorporated at tetrahedral positions in zeolite frameworks.[6, 13-14, 16-19] The peak at ~1125 cm^{-1} represents an additional feature of Ti atoms within the framework; previous studies assign the ~960 and ~1125 cm^{-1} peaks to antisymmetric and symmetric Ti-O-Si vibrations, respectively.[6, 18-20] Figure S6b shows that each Ti-BEA zeolite contains features at ~960 and 1125 cm^{-1}, consistent with the proposal that Ti atoms reside in the *BEA framework. Si-BEA-OH also contains a feature at ~960 cm^{-1}, likely resulting from contributions of silanol defects as reported in literature. Collectively, the Raman spectra suggest that Ti atoms predominately reside at tetrahedral framework positions within the *BEA zeolite framework.

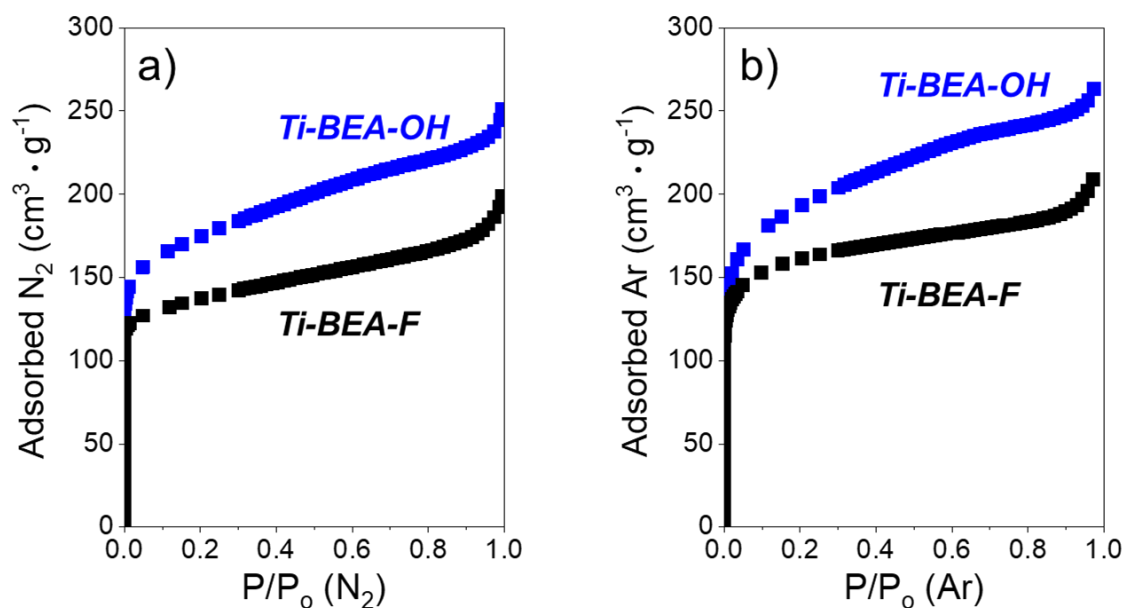**S1.4 N_2, Ar, H_2O, and CH_3OH Adsorption Isotherms over Ti-BEA Materials**

Figure S4. a) N_2 (77 K) and b) Ar (87 K) adsorption isotherms over Ti-BEA-OH (blue) and Ti-BEA-F (black). The samples were degassed under dynamic vacuum prior to adsorption ($< 7 \times 10^{-4}$ Pa, 673 K, 3 h).

The BET surface areas and micropore volumes reported in Table 1 of the main text were calculated from the adsorption isotherms in Figure S4. The values in Table 1 are consistent with previous reports of surface areas[21-23] and micropore volumes[22, 24-27] of *BEA zeolites, supporting that Ti-BEA-OH and Ti-BEA-F possess the *BEA framework.

The BET surface area of Ti-BEA-OH exceeds Ti-BEA-F by ~1.2 times for each method, while the micropore volume is ~1.1 times greater in Ti-BEA-OH for N_2 adsorption and nearly identical between the zeolites for Ar adsorption. While the external surface areas of Ti-BEA-OH are ~2 times greater than Ti-BEA-F, the total pore volumes (micropore + mesopore) differ by < 1.25 times between zeolites for each adsorption measurement (Table S1).

Catalyst	External Surface Area (N_2) (m² g⁻¹)	External Surface Area (Ar) (m² g⁻¹)	BET Surface Area (N_2) (m² g⁻¹)	Micropore Volume (N_2) (m² g⁻¹)	Total Pore Volume (N_2) (cm³ g⁻¹)	Total Pore Volume (Ar) (cm³ g⁻¹)
Ti-BEA-OH	200	177	653	0.184	0.389	0.521
Ti-BEA-F	109	79	528	0.166	0.307	0.583

Table S1. External surface areas and mesopore volumes of Ti-BEA materials obtained from N_2 and Ar physisorption isotherms.

S1.5 Infrared Spectra of Ti-BEA Materials to Measure Silanol Density
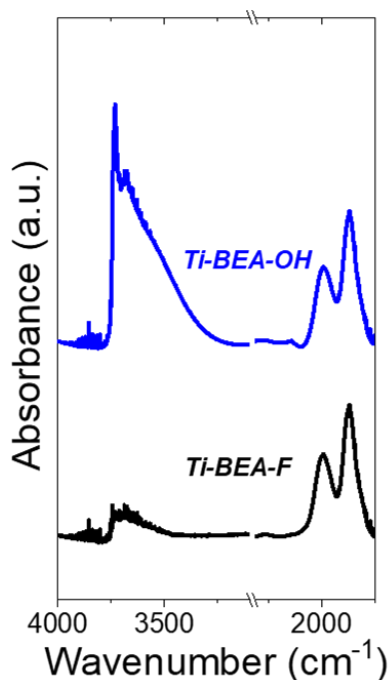

Figure S5. Infrared spectra of dehydrated samples of Ti-BEA-OH (blue) and Ti-BEA-F (black) used for this study. The samples were dehydrated under flowing He (101 kPa He, 50 cm^3 min^{-1}) at 573 K prior to measurement. Spectra are vertically offset for clarity.

The significant difference in the v(O-H) area (3300-3750 cm^{-1}), with respect to the relatively unchanging v(Si-O-Si) area (1800-2100 cm^{-1}), shows that Ti-BEA-OH contains a much greater density of $(SiOH)_x$ groups than Ti-BEA-F (i.e., more hydrophilic). Φ_{IR} in Table 1 of the main text values were calculated by peak fitting on Origin 2021 (OriginLab Corporation). The peak areas for v(O-H) and v(Si-O-Si) are shown in Table S1 and were calculated with Gaussian fits, as illustrated in Figures S6 and S7. During peak fitting, the peak areas were fixed at the values shown in Table S2.

Ti-BEA-OH		Ti-BEA-F	
Peak Center (cm^{-1})	Integrated Area	Peak Center (cm^{-1})	Integrated Area
3731	32.1	3709	11.7
3679	93.4	3620	24.8
3551	207.5	1993	57.9
1990	52.8	1868	79.0
1868	81.2		

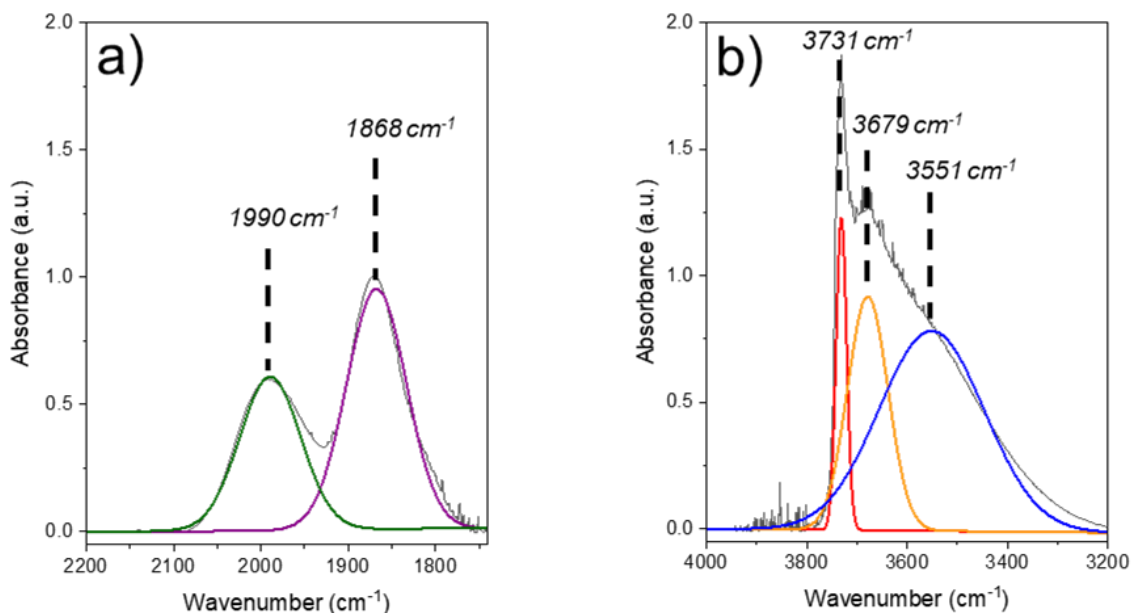**Table S2.** Peak areas for fitted peaks from IR spectra of Ti-BEA samples.

Figure S6. Fitted peaks for the a) Si-O-Si overtones at 1865 (purple) and 2000 cm⁻¹ (green) and b) isolated (red) and networked (blue, orange) Si-OH regions for Ti-BEA-OH.
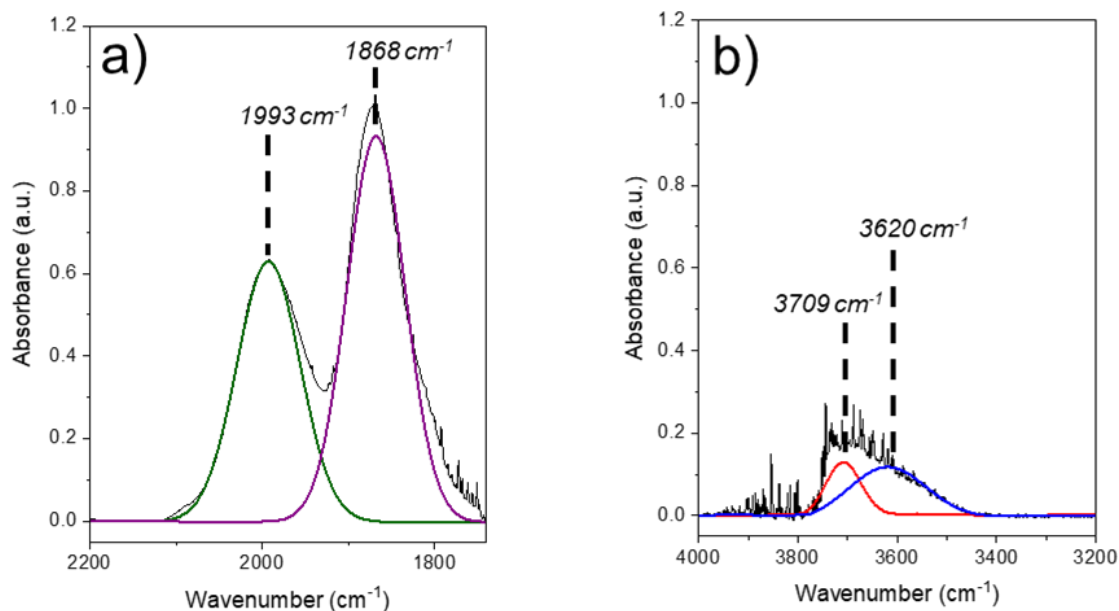

Figure S7. Fitted peaks for the a) Si-O-Si overtones at 1865 (purple) and 2000 cm⁻¹ (green) and b) isolated (red) and networked (blue) Si-OH regions for Ti-BEA-F.

As shown in Equation 1 in the main text, the equation to calculate Φ_{IR} is:

$$\Phi_{IR} = \frac{A_{v(O-H)}}{A_{v(Si-O-Si)}} \tag{S1}$$

The blue and yellow peaks represent networked SiOH features which are summed to determine $A_{v(O-H)}$ for Ti-BEA-OH; only the blue peak was used in $A_{v(O-H)}$ for Ti-BEA-F. The green and purple peaks in the Si-O-Si region were summed together to get $A_{v(Si-O-Si)}$. The red peaks in v(O-H) represent isolated SiOH features, so these peak areas were excluded from the Φ_{IR} calculations. Substituting the areas to Equation S1 gives Φ_{IR} values of 2.25 and 0.27 for Ti-BEA-OH and Ti-BEA-F, respectively.

S1.6 Calculation of $(SiOH)_x$ (unit cell)$^{-1}$ in Ti-BEA-OH

The density of $(SiOH)_x$ per unit cell in Ti-BEA-OH was estimated based on the initial quantity of Al present in the commercial zeolite ($Si:Al = 20$). A BEA unit cell contains 64 heteroatoms (i.e., Si, Al, or Ti), so the initial quantity of Al per unit cell equals 3.047:

$$Al + Si = 64 \quad \longrightarrow \quad Al + 20Al = 64 \quad \longrightarrow \quad \boldsymbol{Al = 3.047}$$

Assuming that all Al atoms are removed, the dealumination produces 3.047 $(SiOH)_x$ (unit cell)$^{-1}$. The Ti weight loading was measured as 0.355% from EDXRF, which gives a Si/Ti ratio of 219. This can be used to calculate the number of Ti atoms per unit cell incorporated into the formed $(SiOH)_4$:

$$Ti + Si = 64 \quad \longrightarrow \quad Ti + 219Ti = 64 \quad \longrightarrow \quad \boldsymbol{Ti = 0.292}$$

The final $(SiOH)_x$ (unit cell)$^{-1}$ is equal to the quantity of removed Al subtracted by the added Ti:

$$(SiOH)_x = removed\ Al - added\ Ti = \boldsymbol{2.75\ (SiOH)_x\ per\ unit\ cell}$$

Ti-BEA-F was synthesized hydrothermally without Al present, so we cannot make the same calculation of $(SiOH)_x$ (unit cell)$^{-1}$.

S2. ¹H NMR Spectroscopy to Calculate Intrapore Solvent Composition

The ratio of the peak areas for H_2O and the organic solvent was calculated for each sample. Then, the known initial mole fraction of H_2O ($x_{H_2O,bulk,initial}$) and organic solvent and peak area ratios before ($A_{H_2O:org,initial}$) and after ($A_{H_2O:org,final}$) contact with Ti-BEA were used to calculate the final bulk solvent fractions:

$$x_{H_2O,bulk,final} = x_{H_2O,bulk,initial} * \frac{A_{H_2O:org,final}}{A_{H_2O:org,initial}} \tag{S2}$$

$$x_{org,bulk,final} = 1 - x_{H_2O,bulk,final} \tag{S3}$$

The intrapore solvent fraction was then calculated, starting by estimating the fraction of solvent adsorbed from the bulk solvent ($V_{solvent,ads}$) and the fraction of the initial solvent volume remaining in the bulk solvent after adsorption ($x_{bulk,final}$):

$$V_{solvent,ads} = m_{zeolite} * V_{pore,^*BEA} \tag{S4}$$

$$x_{bulk,final} = 1 - \left(\frac{V_{solvent,ads}}{V_{solvent,total}} \right) \tag{S5}$$

where $m_{zeolite}$ is the mass of Ti-BEA added to the solvent and $V_{pore,^*BEA}$ is the pore volume of Ti-BEA-OH or Ti-BEA-F (Section S1.5).

From there, the intrapore molar ratio ($\frac{n_{H_2O,pore}}{n_{org,pore}}$) and H_2O fraction ($x_{H_2O,pore}$) can be calculated:

$$\frac{n_{H_2O,pore}}{n_{org,pore}} = \frac{x_{H_2O,bulk,initial} - (x_{bulk,final}*x_{H_2O,bulk,final})}{x_{org,bulk,initial} - (x_{org,final}*x_{org,bulk,final})} \tag{S6}$$

$$x_{H_2O,pore} = \frac{\frac{n_{H_2O,pore}}{n_{org,pore}}}{1 - \frac{n_{H_2O,pore}}{n_{org,pore}}} \tag{S7}$$

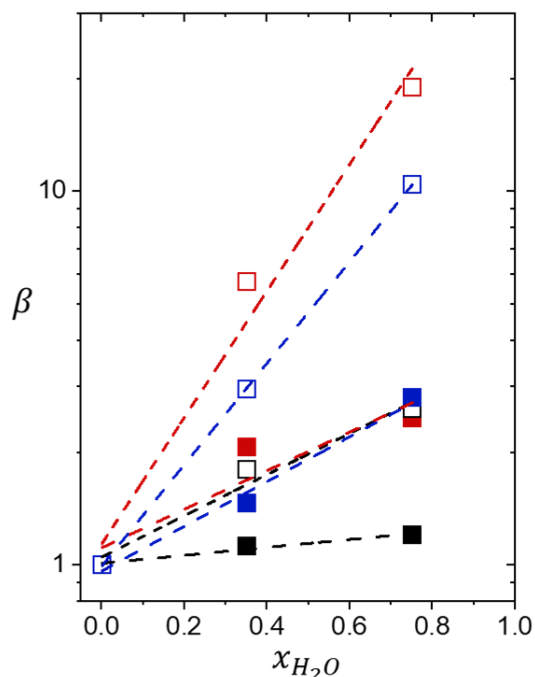## S3. H₂O₂ Selectivity Dependences on H₂O Fraction

Figure S8. Relative H_2O_2 selectivities (β) for epoxidation (1 mM C_6H_{12}, 10 mM H_2O_2 (with 39 mM H_2O), 313 K) as a function of H_2O mole fraction (x_{H_2O}) in mixtures of CH_3CN (■,□), CH_3OH (■,□), and $C_4H_6O_2$ (■,□) with H_2O over Ti-BEA-OH (solid points) and Ti-BEA-F (hollow points).

The relative H_2O_2 selectivity (β) plotted in Figure S8 is defined as:

$$\beta = \frac{S_{H_2O_2,x}}{S_{H_2O_2,0.002}} \tag{S8}$$

which equals the ratio of H_2O_2 selectivities for epoxidation over H_2O_2 decomposition at $x_{H_2O} = x$ ($S_{H_2O_2,x}$) and $x_{H_2O} = 0.002$ ($S_{H_2O_2,0.002}$). This selectivity ratio quantifies the magnitude of H_2O_2 selectivity increases for C_6H_{12} epoxidation upon adding more H_2O to the organic solvent. In general, Ti-BEA-F shows greater increases in the relative H_2O_2 selectivity than Ti-BEA-OH at a higher x_{H_2O}. Among organic solvents, CH_3CN shows the smallest increases in relative selectivity, while CH_3OH and $C_4H_6O_2$ show similar magnitudes of relative selectivity increases. Overall, the data in Figure S8 and Figure 1c of the main text show that adding more H_2O allows CH_3OH and $C_4H_6O_2$ mixtures to yield more similar selectivities to the best-performing organic solvent, CH_3CN.

S4. Turnover Rates as Functions of [C_6H_{12}], [H_2O_2], and x_{H_2O} for CH_3CN and $C_4H_6O_2$ Mixtures
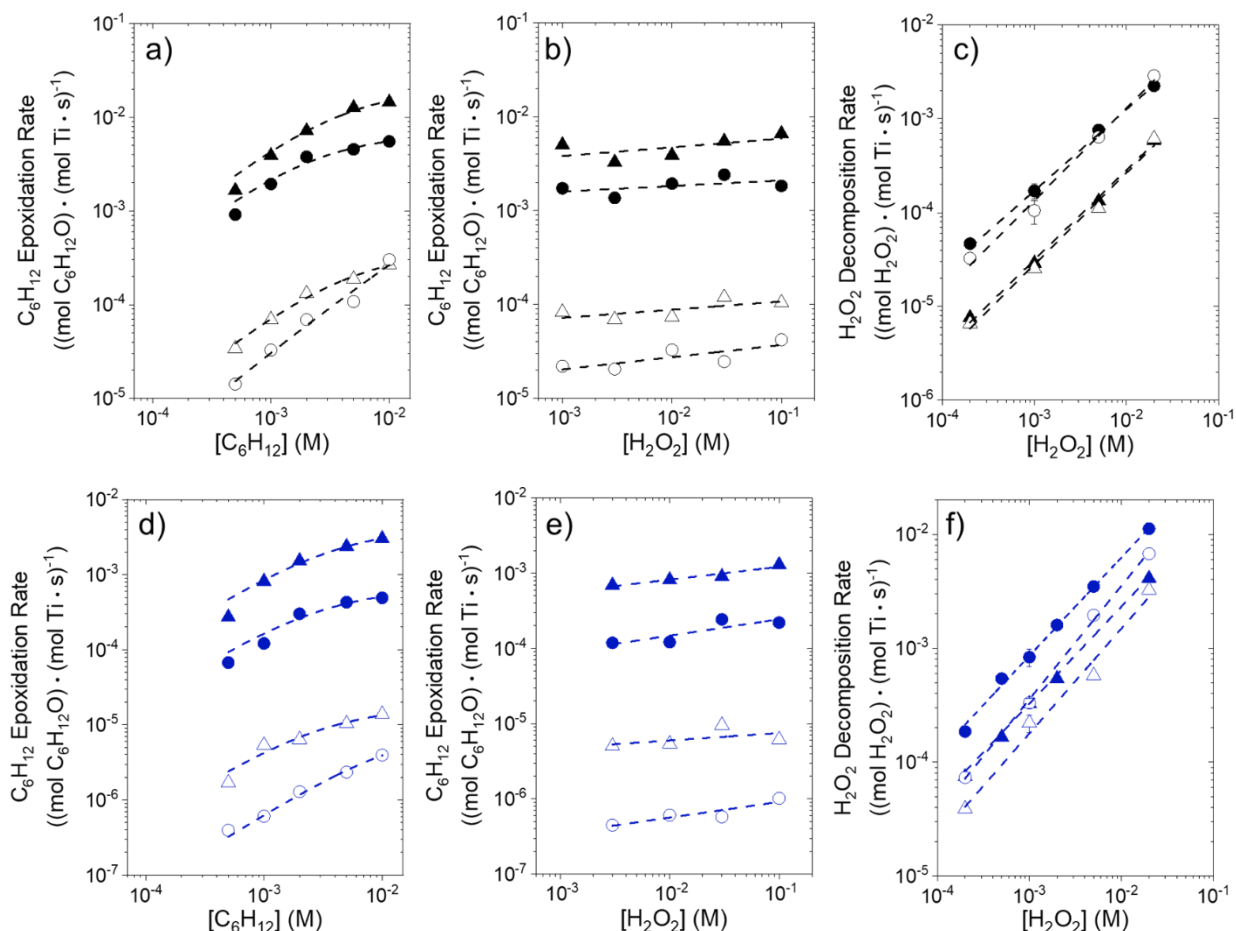

Figure S9. Turnover rates for C_6H_{12} epoxidation as a function of a,d) C_6H_{12} concentration (10 mM H_2O_2, 313 K) and b,e) H_2O_2 concentration (1 mM C_6H_{12}, 313 K) and turnover rates for c,f) H_2O_2 decomposition (313 K) as a function of H_2O_2 concentration for a,b,c) CH_3CN mixtures containing $x_{H_2O} = 0.002$ (39 mM) (●,○) or $x_{H_2O} = 0.75$ (~27.8 M) (▲,△) and d,e,f) $C_4H_6O_2$ mixtures containing $x_{H_2O} = 0.002$ (●,○) or $x_{H_2O} = 0.75$ (~23.0 M) (▲,△) over Ti-BEA-OH (solid points) and Ti-BEA-F (hollow points).

Figure S9 reveals that C_6H_{12} epoxidation turnover rates in CH_3CN and $C_4H_6O_2$ mixtures with H_2O show a linear dependence on [C_6H_{12}] (Figures S9a and S9d) and nearly zero-order dependence on [H_2O_2] (Figures S9b and S9e) at low ratios of [C_6H_{12}] to [H_2O_2]. H_2O_2 decomposition rates show a linear dependence on [H_2O_2] at all H_2O_2 concentrations examined (Figures S9c and S9f). The rate dependences match those shown for CH_3OH mixtures in Figure 2 of the main text. These data indicate that the reaction mechanisms for C_6H_{12} epoxidation and H_2O_2 decomposition do not change with the organic solvent, x_{H_2O}, or $(SiOH)_x$ density of the zeolite.

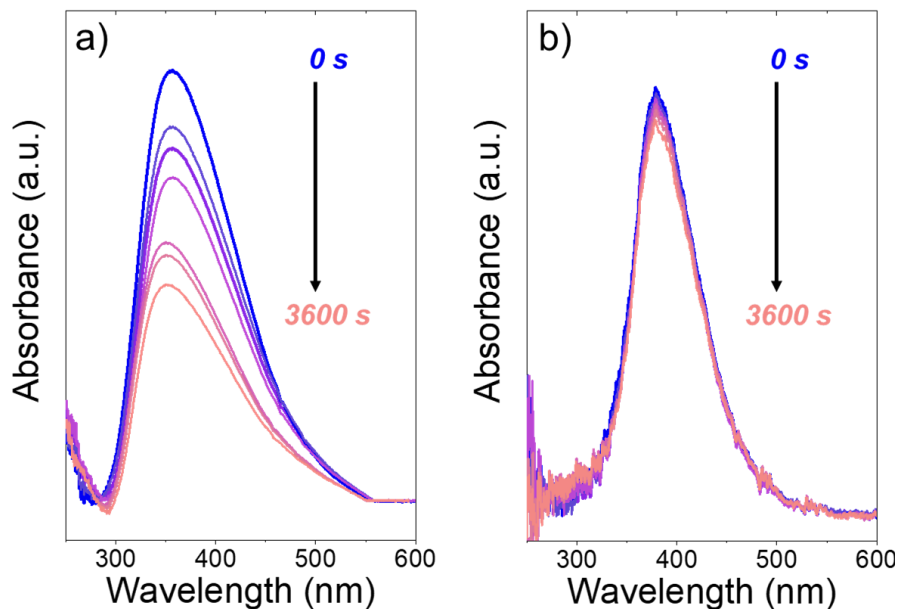## S5. *In situ* UV-Vis Spectroscopy to Examine H_2O_2 Activation over Ti-BEA Materials

Figure S10. *In situ* UV-Vis spectra of Ti-BEA-F as a function of time within continuously flowing neat a) H_2O and b) $C_4H_6O_2$ (313 K, 1 cm^3 min^{-1}) after H_2O_2 activation (100 mM H_2O_2 (with 390 mM H_2O), 313 K, 1 cm^3 min^{-1}). The reported spectra were taken every 600 s after H_2O_2 activation.

The absorbance features from 300 – 550 nm in Figure S10 in Ti-BEA-F match those observed in Ti-BEA-OH (Figure 3, main text) and indicate that each Ti-BEA activates H_2O_2 to form a pool of Ti-OOH and Ti-(η^2)-O_2 in H_2O and $C_4H_6O_2$.[24, 28-29] These absorbance features occur in the same region as previously reported over Ti-BEA in CH_3CN[28-29] and CH_3OH.[24] The attenuation of the peak areas for Ti-OOH and Ti-(η^2)-O_2 with time in H_2O and negligible changes in $C_4H_6O_2$ agree with those in Ti-BEA-OH. The peak areas attenuate by ~45% in H_2O ~5% in $C_4H_6O_2$ over 1 h. The slight decrease in features over $C_4H_6O_2$ with time may result from residual H_2O remaining in the pores from the aqueous H_2O_2 solution (390 mM H_2O) or reaction between $C_4H_6O_2$ molecules and the H_2O_2-derived intermediates. These trends suggest that the reversibility of H_2O_2 activation does not depend on the $(SiOH)_x$ density of Ti-BEA.

Figure S11 displays the evolution of the peak areas for H_2O_2-derived intermediates with time after cutting off H_2O_2 flow over Ti-BEA-OH in H_2O (Figure S11a), equimolar H_2O and $C_4H_6O_2$ (Figure S11b), and over Ti-BEA-F in H_2O (Figure S11c). The data plots were fit to exponential decay functions to yield rate constants for desorption of Ti-OOH and Ti-(η^2)-O_2 (k_{-3}), shown in Table S3. Neat H_2O and equimolar H_2O and $C_4H_6O_2$ provide k_{-3} values that exceed neat $C_4H_6O_2$ by more than an order of magnitude, reinforcing that protic solvents facilitate reversible activation of H_2O_2 over Ti-BEA materials.
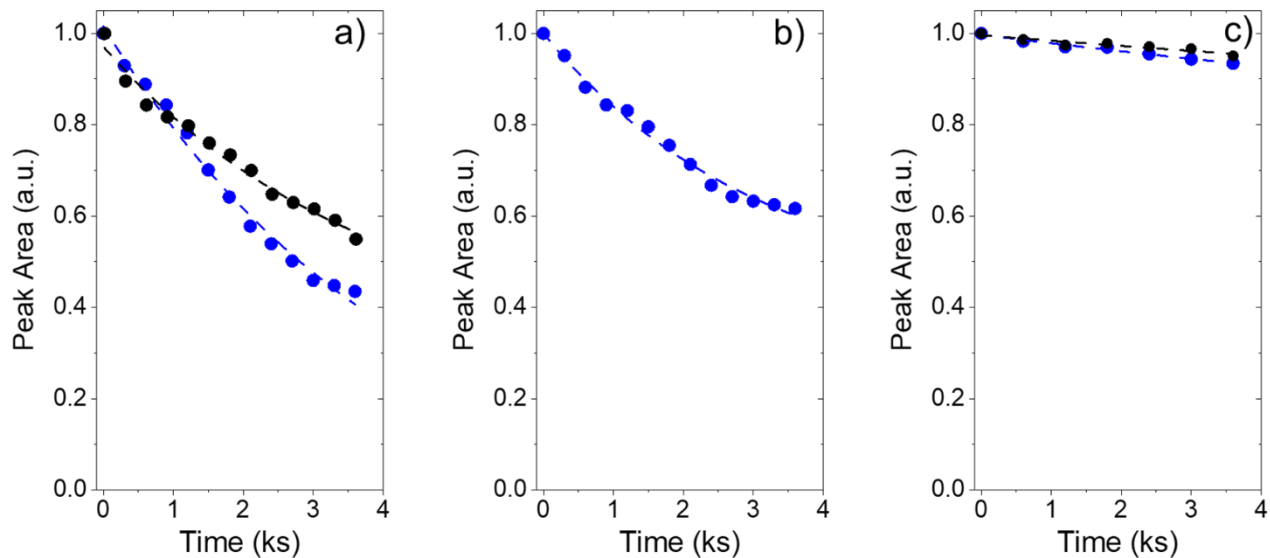
Figure S11. Normalized H_2O_2-derived intermediate peak areas as a function of time after H_2O_2 activation after H_2O_2 activation (100 mM H_2O_2 (with 390 mM H_2O), 313 K, 1 cm^3 min^{-1}) within continuously flowing neat a) H_2O, b) equimolar H_2O and $C_4H_6O_2$, c) and neat $C_4H_6O_2$ (313 K, 1 cm^3 min^{-1}) over Ti-BEA-OH (blue) and Ti-BEA-F (black). The dashed lines represent fits to an exponential decay function for first-order kinetics.

Solvent	Ti-BEA-OH k_{-3} (ks^{-1})	Ti-BEA-F k_{-3} (ks^{-1})
H_2O	0.43 ± 0.06	0.47 ± 0.08
$H_2O/C_4H_6O_2$	0.56 ± 0.07	--
$C_4H_6O_2$	0.03 ± 0.03	0.02 ± 0.06

Table S3. Rate constants for the re-formation of H_2O_2 from H_2O_2-derived intermediates (k_{-3}) over Ti-BEA zeolites. k_{-3} values and uncertainties are calculated from the exponential fits in Figure S11.

S6. Derivation of Rate Expression for 1-Hexene Epoxidation over Ti-BEA Materials

Scheme 1 in the main text shows the elementary steps for 1-hexene (C_6H_{12}) epoxidation and H_2O_2 decomposition.[29] The mechanism begins with the quasi-equilibrated adsorption of a solvent molecule (step 0), C_6H_{12} (step 1), or H_2O_2 (step 2). H_2O_2 then irreversibly activates to form Ti-OOH (step 3).[29-30] The Ti-OOH intermediate may then react with another H_2O_2 molecule in H_2O_2 decomposition (step 6), react with a C_6H_{12} molecule in the kinetically relevant step for epoxidation (step 4), or desorb to re-form H_2O_2 (reverse of step 3). The epoxide that forms undergoes quasi-equilibrated desorption to form the 1,2-epoxyhexane ($C_6H_{12}O$) product. Epoxidation turnover rates can be modeled with Equation 3 from the main text:

$$r_{epox} = k_4[Ti - OOH][C_6H_{12}] \tag{S9}$$

where r_E is the epoxidation rate, k_4 is the rate constant for step 4 in Scheme 1, and [Ti-OOH] and [C_6H_{12}] represent the number of H_2O_2-activated metal sites and C_6H_{12} molecules in the liquid phase.

Applying the pseudo-steady state hypothesis to the Ti-OOH intermediate gives:

$$r_{epox} = \frac{k_3 k_4 K_2 [C_6H_{12}][H_2O_2][*]}{k_{-3} + k_4[C_6H_{12}] + k_6[H_2O_2]} \tag{S10}$$

The total number of Ti active sites ([L]) can be written as:

$$[L] = [S*] + [C_6H_{12}*] + [H_2O_2*] + [OOH*] + [C_6H_{12}O*] \tag{S11}$$

where [S*] is the number of sites occupied by a solvent molecule (S; CH_3CN, CH_3OH, $C_4H_6O_2$, or H_2O) and the other terms represent the number of adsorbed reactants and products. Substituting rate constants, equilibrium constants, and reactant and product concentrations gives:

$$[L] = K_0[S] + K_1[C_6H_{12}] + K_2[H_2O_2] + \frac{k_3 K_2 [H_2O_2]}{k_{-3} + k_4[C_6H_{12}] + k_6[H_2O_2]} + \frac{[C_6H_{12}O]}{K_5} \tag{S12}$$

Combining Equations S10 and S12 gives the full rate expression (Equation 4 in the main text):

$$\frac{r_{epox}}{[L]} = \frac{\frac{k_3 k_4 K_2 [C_6H_{12}][H_2O_2]}{k_{-3} + k_4[C_6H_{12}] + k_6[H_2O_2]}}{K_0[S] + K_1[C_6H_{12}] + K_2[H_2O_2] + \frac{k_3 K_2 [H_2O_2]}{k_{-3} + k_4[C_6H_{12}] + k_6[H_2O_2]} + \frac{[C_6H_{12}O]}{K_5}} \tag{S13}$$

When molar ratios of H_2O_2 to C_6H_{12} exceed two, rates depend linearly on [C_6H_{12}] and negligibly on [H_2O_2] (Figure 2 in main text and Figure S9), indicating that Ti-OOH intermediates saturate Ti sites. The [OOH*] term dominates in the denominator under these conditions, and all other terms can be canceled out. Equation S13 then simplifies to the same form as Equation 5 in the main text:

$$\frac{r_{epox}}{[L]} = k_4[C_6H_{12}] \tag{S14}$$

Equation S14 describes the kinetic regime under which activation barriers were measured. Under conditions in which the active sites are saturated with the epoxide product, the [$C_6H_{12}O*$] term dominates in the denominator of Equation S13, which instead simplifies to:

$$\frac{r_{epox}}{[L]} = \frac{k_3 k_4 K_2 K_5 [C_6H_{12}][H_2O_2]}{[C_6H_{12}O](k_{-3} + k_4[C_6H_{12}] + k_6[H_2O_2])} \tag{S15}$$

When materials show high H_2O_2 selectivities towards epoxidation (i.e., $S_{H_2O_2} > 90\%$), the rate of epoxidation far exceeds H_2O_2 decomposition (i.e., $k_4[C_6H_{12}] \gg k_6[H_2O_2]$). Combining this with a solvent

that shows negligible re-formation rates of H_2O_2 from Ti-OOH (e.g., CH_3CN or $C_4H_6O_2$ with minimal quantities of H_2O), where the value of the quantity $k_4[C_6H_{12}]$ is much greater than k_{-3}, allows for further simplification of Equation S15:

$$\frac{r_{epox}}{[L]} = \frac{k_3K_2K_5[H_2O_2]}{[C_6H_{12}O]} \tag{S16}$$

Equation S16 matches previous reports from our group in which rates of C_6H_{12}[29] and C_6H_{10}[28] epoxidation over Ti-BEA in CH_3CN solvent depend negligibly on the concentration of the alkene substrate, linearly on the concentration of H_2O_2, and inversely on the epoxide concentration when the alkene is present in significant excess to H_2O_2 (i.e., molar ration of alkene to H_2O_2 greater than 50).

Equation 6 in the main text shows the expression for H_2O_2 decomposition rates:

$$-r_{decomp} = k_6[Ti-OOH][H_2O_2] \tag{S17}$$

Substituting terms for [Ti-OOH] and using the site balance for [L] leads to (Equation 7 in the main text):

$$-\frac{r_{decomp}}{[L]} = \frac{\frac{k_3k_4K_2[H_2O_2]^2}{k_{-3}+k_4[C_6H_{12}]+k_6[H_2O_2]}}{K_0[S]+K_1[C_6H_{12}]+K_2[H_2O_2]+\frac{k_3K_2[H_2O_2]}{k_{-3}+k_4[C_6H_{12}]+k_6[H_2O_2]}+\frac{[C_6H_{12}O]}{K_5}} \tag{S18}$$

At the low ratios of $[C_6H_{12}]:[H_2O_2]$ used when measuring activation barriers, Ti-OOH saturates the Ti-BEA surface and H_2O_2 decomposition rates increase linearly with $[H_2O_2]$.[28] This allows us to simplify Equation S18 to:

$$-\frac{r_{decomp}}{[L]} = k_6[H_2O_2] \tag{S19}$$

Activation parameter equations for H_2O_2 decomposition can be derived in an identical procedure as shown for C_6H_{12} epoxidation in Section 3.4 of the main text. The apparent activation free energy ($\Delta G_{app}^{\ddagger}$) equals the difference between the free energy of the transition state and reference state components:

$$\Delta G_{app,decomp}^{\ddagger} = \left(G_{decomp}^{\ddagger,0} + G_{decomp}^{\ddagger,\varepsilon}\right) - \left(G_{Ti-OOH}^{0} + G_{Ti-OOH}^{\varepsilon}\right) - \left(G_{H_2O_2}^{0} + G_{H_2O_2}^{\varepsilon}\right) \tag{S20}$$

An apparent free energy term ($\Delta G^*_{app}{}^{\ddagger}$) excluding the activity coefficient of H_2O_2 corresponds to the k_6^* term introduced in Equation 10 of the main text, which originates from the rate constant for H_2O_2 decomposition (k_6):

$$k_6^* = \frac{k_BT}{h}\exp\left(-\frac{\Delta G^*_{app,decomp}{}^{\ddagger}}{RT}\right) \tag{S21}$$

To obtain $\Delta G^*_{app,decomp}{}^{\ddagger}$, we add $G_{H_2O_2}^{\varepsilon}$ to each side of Equation S20:

$$\Delta G^*_{app,decomp}{}^{\ddagger} = \Delta G_{app,decomp}^{\ddagger} + G_{H_2O_2}^{\varepsilon} = \left(G_{decomp}^{\ddagger,0} + G_{decomp}^{\ddagger,\varepsilon}\right) - \left(G_{Ti-OOH}^{0} + G_{Ti-OOH}^{\varepsilon}\right) - G_{H_2O_2}^{0} \tag{S22}$$

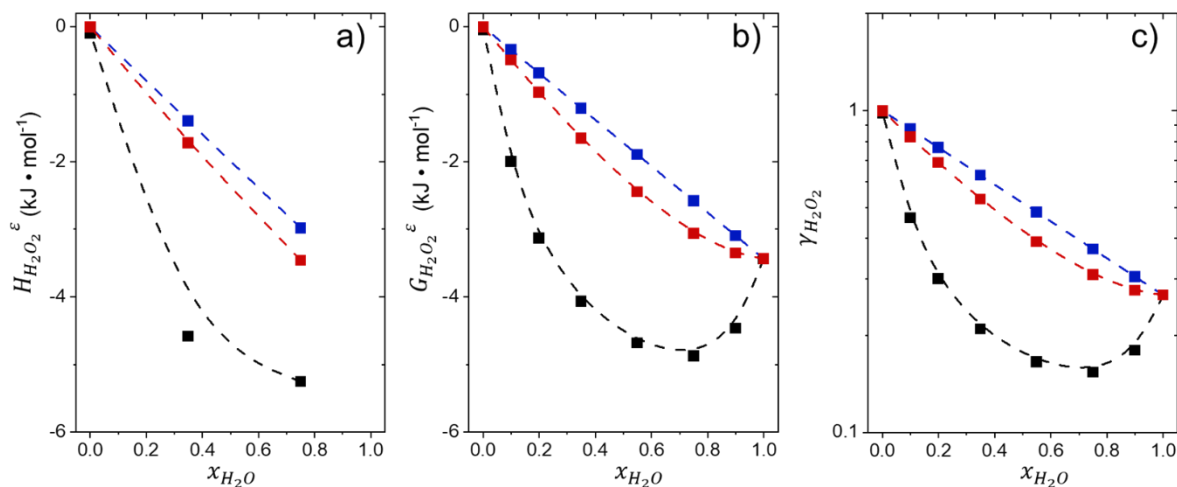## S7. Excess Energies to Probe Changes in Fluid Phase C₆H₁₂ and H₂O₂ Stability

Figure S12. a) Excess enthalpies ($H_{H_2O_2}^{\varepsilon}$) (308 − 338 K), b) excess free energies ($G_{H_2O_2}^{\varepsilon}$) (313 K), and c) activity coefficients of H₂O₂ ($\gamma_{H_2O_2}$) (313 K) as a function of x_{H_2O} in mixtures of CH₃CN (■), CH₃OH (■), and C₄H₆O₂ (■) with H₂O. Activity coefficients for H₂O₂ were obtained with the NRTL method on ChemCAD.
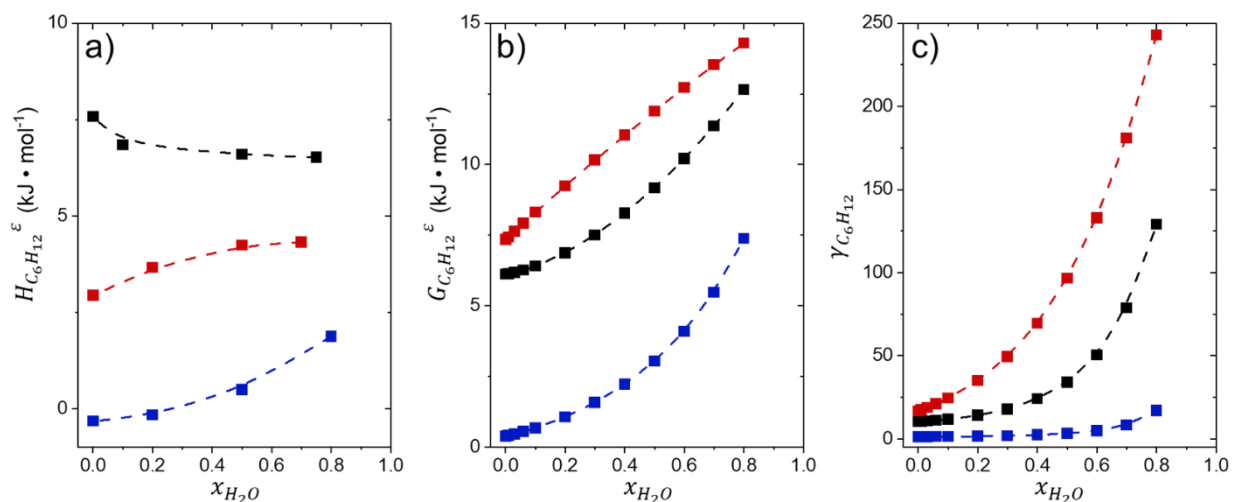

Figure S13. a) Excess enthalpies ($H_{C_6H_{12}}^{\varepsilon}$) (308 − 338 K), b) excess free energies ($G_{C_6H_{12}}^{\varepsilon}$) (313 K), and c) activity coefficients of C₆H₁₂ ($\gamma_{C_6H_{12}}$) (313 K) as a function of x_{H_2O} in mixtures of CH₃CN (■), CH₃OH (■), and C₄H₆O₂ (■) with H₂O. Activity coefficients for C₆H₁₂ were obtained with the Volume-Translated Peng-Robinson (VTPR) method on ChemCAD.

Figure S12 and S13 show excess energies and activity coefficients for C₆H₁₂ and H₂O₂, respectively. The equations to compute the excess energies from the activity coefficients are as follows:

$$G_j^{\varepsilon} = RT * ln(\gamma_j) \tag{S23}$$

$$H_j^{\varepsilon} = -RT^2 * \frac{d\,ln(\gamma_j)}{dT} \tag{S24}$$

where j represents C₆H₁₂ or H₂O₂ here, R equals the ideal gas constant, and T represents temperature. The differential term $\left(\frac{d\,ln(\gamma_j)}{dT}\right)$ was obtained by calculating activity coefficients between 308-333 K by

increments of 5 K. The natural log of the activity coefficients was plotted against the temperature, and the slope of this line equaled the differential term (examples shown in Figure S14).
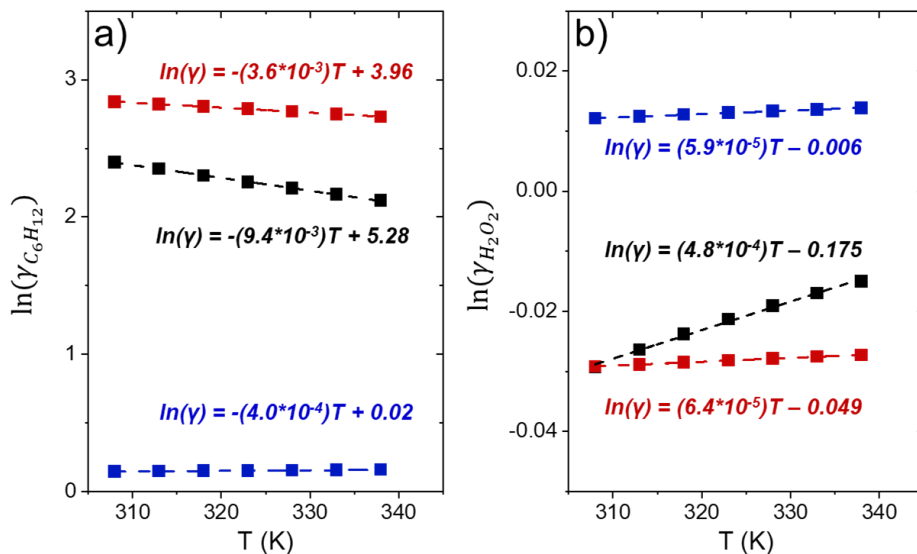

Figure S14. Natural logs of the activity coefficient of a) C_6H_{12} and b) H_2O_2 as a function of temperature (308 – 338 K) in CH_3CN (■), CH_3OH (■), and $C_4H_6O_2$ (■) with 39 mM H_2O ($x_{H_2O} = 0.002$). Activity coefficients were obtained with the Volume-Translated Peng-Robinson (VTPR) method for C_6H_{12} and the UNIQUAC method for H_2O_2 on ChemCAD.

S8. C₆H₁₂ Epoxidation and H₂O₂ Decomposition Rates Normalized by Reactant Activity Coefficients

Changing x_{H_2O} affects the stability of fluid phase C_6H_{12}, so rates were normalized by C_6H_{12} activity coefficients to examine the effect of C_6H_{12} stability on epoxidation rates (Figure 3a). An expression for normalized C_6H_{12} epoxidation rates can be obtained by starting with the expression for epoxidation rates (Equation S9). Using transition state theory,[31-32] we can define an alternate rate expression for epoxidation, an equilibrium constant between the transition state and reference state ($K^{\ddagger epox}$), and a new expression for the rate constant k_4:

$$r_{epox} = k_4[\ddagger_{epox}] \tag{S25}$$

$$K^{\ddagger epox} = \frac{a_{\ddagger}}{a_{C_6H_{12}} a_{Ti-OOH}} = \frac{\gamma_{\ddagger epox}[\ddagger_{epox}]}{\gamma_{C_6H_{12}}[C_6H_{12}]\gamma_{Ti-OOH}[Ti-OOH]} \tag{S26}$$

$$k_4 = \frac{k_B T}{h} K^{\ddagger epox} \tag{S27}$$

where $[\ddagger_{epox}]$ is the concentration of transition state complexes, a_i is the activity of a component, and γ_i is the activity coefficient of a component. We can substitute the expressions for $K^{\ddagger epox}$ and k_4 into Equation S25:

$$r_{epox} = \frac{k_B T}{h} K^{\ddagger epox} \frac{\gamma_{C_6H_{12}}\gamma_{Ti-OOH}[C_6H_{12}][Ti-OOH]}{\gamma_{\ddagger epox}} \tag{S28}$$

Under conditions where Ti-OOH is the MARI, [L] = [Ti-OOH]. Substituting in [L] and dividing by [L] and $\gamma_{C_6H_{12}}$ yields the final expression for activity-normalized turnover rates:

$$\frac{r_{epox}}{[L]*\gamma_{C_6H_{12}}} = \frac{k_B T}{h} K^{\ddagger epox} \frac{\gamma_{Ti-OOH}[C_6H_{12}]}{\gamma_{\ddagger epox}} \tag{S29}$$

Changing [H₂O] also alters the stability of fluid phase H₂O₂, so H₂O₂ decomposition rates were normalized by H₂O₂ activity coefficients (Figure 3b). Again, invoking transition theory, we obtain a normalized decomposition rate expression with an identical form to Equation S28:

$$-r_{decomp} = \frac{k_B T}{h} K^{\ddagger decomp} \frac{\gamma_{H_2O_2}\gamma_{Ti-OOH}[H_2O_2][Ti-OOH]}{\gamma_{\ddagger decomp}} \tag{S30}$$

When Ti-OOH saturates the active sites, the expression simplifies to:

$$\frac{-r_{decomp}}{[L]*\gamma_{H_2O_2}} = \frac{k_B T}{h} K^{\ddagger decomp} \frac{\gamma_{Ti-OOH}[H_2O_2]}{\gamma_{\ddagger decomp}} \tag{S31}$$

Several activity coefficients were examined for the rate normalizations, as shown in Figures S15 and S16. The Wilson and NRTL methods give similar activity coefficients for H₂O₂, while the Modified UNIFAC (Dortmund) and VTPR methods give similar activity coefficients for C_6H_{12}. The NRTL and VTPR methods were chosen to report the normalized rates in Figure 3 because of the agreement with another method. The UNIQUAC (Figure S15a) and UNIFAC LLE (Figure S16a) methods gave activity coefficients that did not agree closely with any available methods in ChemCAD.
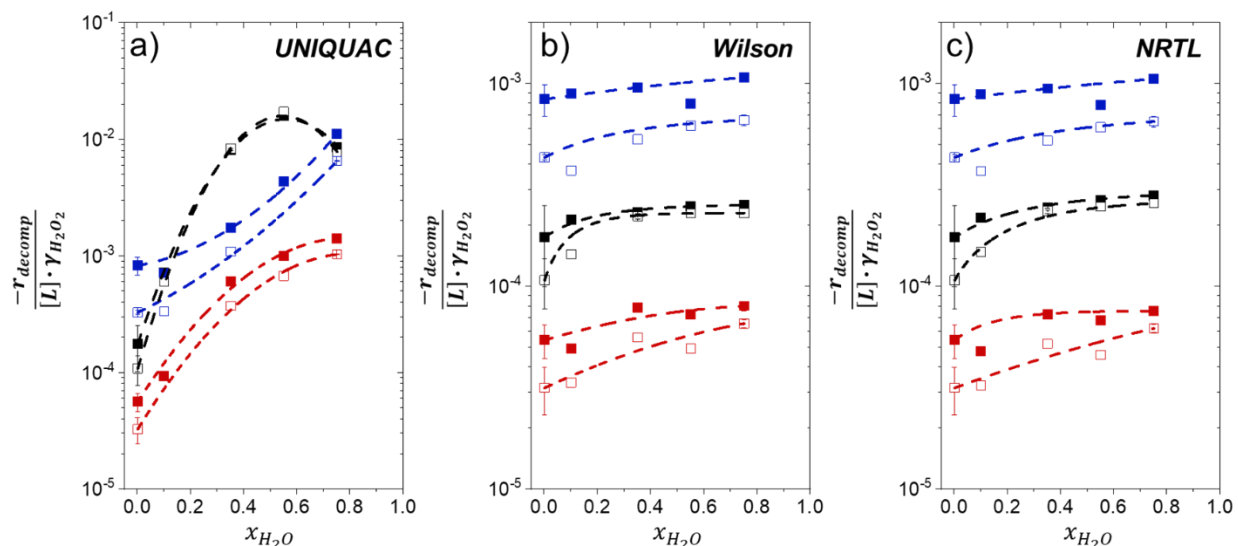
Figure S15. Turnover rates for H_2O_2 decomposition (1 mM H_2O_2, 313 K) normalized by H_2O_2 activity coefficient and as a function of x_{H_2O} in mixtures of CH_3CN (■,□), CH_3OH (■,□), and $C_4H_6O_2$ (■,□) with H_2O over Ti-BEA-OH (solid points) and Ti-BEA-F (hollow points). Activity coefficients of H_2O_2 were calculated using the methods listed in the plot area on ChemCAD.
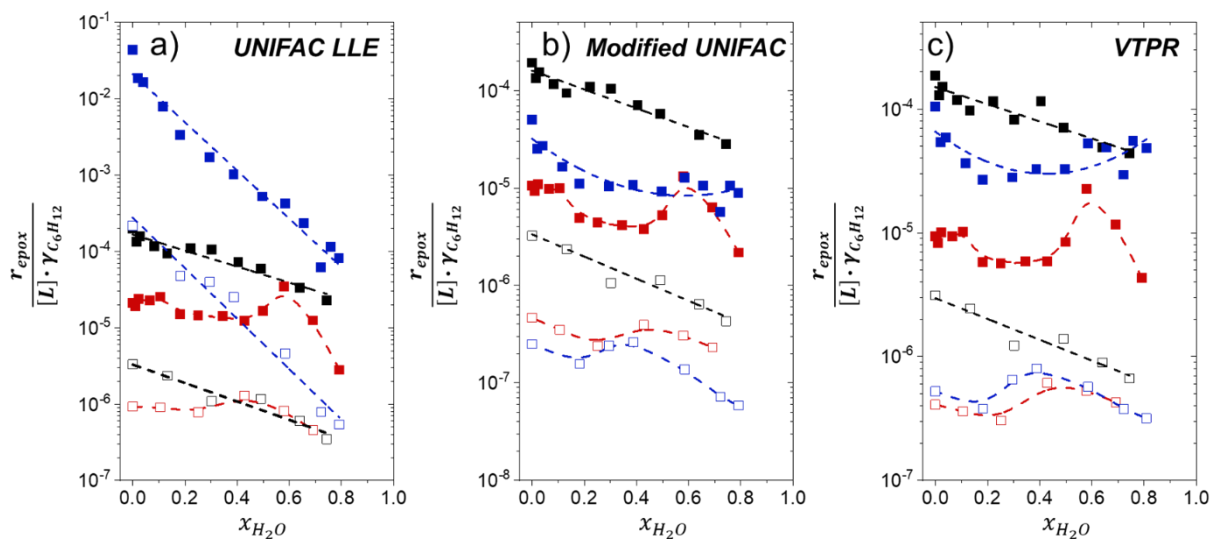

Figure S16. Turnover rates for C_6H_{12} epoxidation (1 mM C_6H_{12}, 10 mM H_2O_2, 313 K) normalized by C_6H_{12} activity coefficient and as a function of x_{H_2O} in mixtures of CH_3CN (■,□), CH_3OH (■,□), and $C_4H_6O_2$ (■,□) with H_2O over Ti-BEA-OH (solid points) and Ti-BEA-F (hollow points). Activity coefficients of C_6H_{12} were calculated using the methods listed in the plot area on ChemCAD.

S9. Activation Enthalpies and Entropies for C_6H_{12} Epoxidation and H_2O_2 Decomposition
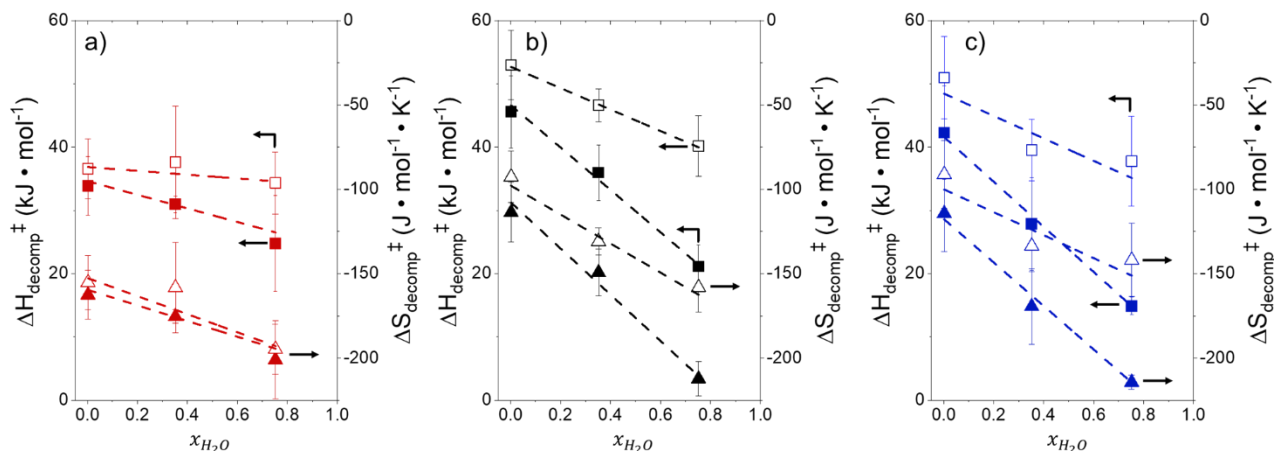
Figure S17. Apparent activation enthalpies (squares) and entropies (triangles) for H_2O_2 decomposition (1 mM H_2O_2, 313-343 K) as a function of x_{H_2O} in mixtures of a) CH_3OH (red), b) CH_3CN (black), and c) $C_4H_6O_2$ (blue) with H_2O over Ti-BEA-OH (solid points) and Ti-BEA-F (hollow points).
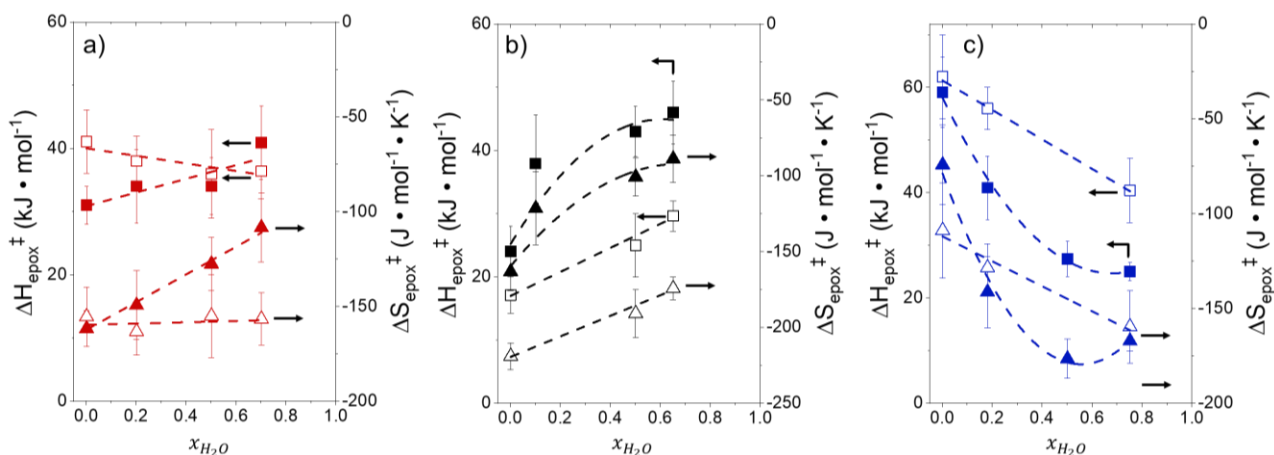
Figure S18. Apparent activation enthalpies (squares) and entropies (triangles) C_6H_{12} epoxidation (1 mM C_6H_{12}, 10 mM H_2O_2, 308-338 K) as a function of x_{H_2O} in mixtures of a) CH_3OH (red), b) CH_3CN (black), and c) $C_4H_6O_2$ (blue) with H_2O over Ti-BEA-OH (solid points) and Ti-BEA-F (hollow points).

Figures S17 and S18 present $\Delta H_{app}^{\ddagger}$ and $\Delta S_{app}^{\ddagger}$ values for C_6H_{12} epoxidation and H_2O_2 decomposition. $\Delta H_{app}^{\ddagger}$ and $\Delta S_{app}^{\ddagger}$ generally trend in the same direction for each reaction, organic solvent, and zeolite. Taken together with the values from Figures 5 and 6, the data in Figure S16 indicate that changes in the enthalpy of the transition states and Ti-OOH intermediate from interactions with solvent molecules couple with compensating changes in entropy. A decrease in enthalpy of a species from solvent interactions (e.g., hydrogen bonding) couples with a decrease in entropy from the same interactions, while solvent interactions that give an increase in enthalpy (e.g., disruption of hydrogen bonds) also give an increase in entropy of that species. However, the enthalpy and entropy changes generally do not offset, leading to differences in $\Delta G_{app}^{\ddagger}$ and rates between organic solvents and zeolites.

The $\Delta H_{app}^{\ddagger}$ and $\Delta S_{app}^{\ddagger}$ values were calculated using van't Hoff analysis. Applying transition state theory and substituting an expression for the apparent free energy to Equations 5 and 8 of the main text yields alternate rate expressions for C_6H_{12} epoxidation and H_2O_2 decomposition:

$$\frac{r_E}{[L]} = \frac{k_B T}{h} \cdot \exp\left(-\frac{\Delta G_{epox}^{\ddagger}}{RT}\right) \cdot [C_6 H_{12}] \tag{S32}$$

$$\frac{r_D}{[L]} = \frac{k_B T}{h} \cdot \exp\left(-\frac{\Delta G_{decomp}^{\ddagger}}{RT}\right) \cdot [H_2 O_2] \tag{S33}$$

Rearranging and substituting in the apparent activation enthalpy and entropy:

$$\ln\left(\frac{r_E}{[L]} \frac{h}{k_B T [C_6 H_{12}]}\right) = \frac{1}{T}\left(\frac{-\Delta H_{epox}^{\ddagger}}{R}\right) + \frac{\Delta S_{epox}^{\ddagger}}{R} \tag{S34}$$

$$\ln\left(\frac{r_D}{[L]} \frac{h}{k_B T [H_2 O_2]}\right) = \frac{1}{T}\left(\frac{-\Delta H_{decomp}^{\ddagger}}{R}\right) + \frac{\Delta S_{decomp}^{\ddagger}}{R} \tag{S35}$$

The natural log term on the left side of Equations S34 and S35 was plotted as the y-axis against inverse temperature as the x-axis. As depicted in Figure S19, a line was fit to this data, and the slope of this line equaled the negative of the apparent activation enthalpy divided by the ideal gas constant, while the y-intercept equaled the apparent activation entropy divided by the ideal gas constant (Table S4).
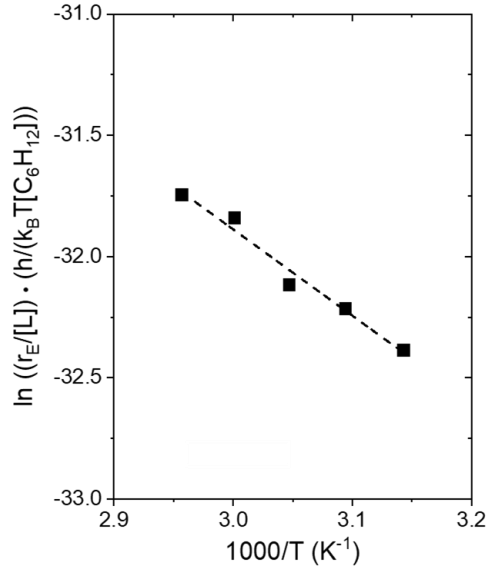
Figure S19. Representative Eyring plot for $C_6 H_{12}$ epoxidation (1 mM $C_6 H_{12}$, 10 mM $H_2 O_2$, 318-338 K) in $x_{CH_3 CN} = 0.35$ (11.7 M) with $H_2 O$ (21.6 M) over Ti-BEA-F.

$\dfrac{-\Delta H_{epox}^{\ddagger}}{R}$	$\dfrac{\Delta S_{epox}^{\ddagger}}{R}$
-3.57 ± 0.32	-21.2 ± 1.0

Table S4. Activation enthalpy and entropy for $C_6 H_{12}$ epoxidation divided by the ideal gas constant, obtained from the slope and intercept, respectively, of Figure S19.

S10. Solvent Properties

Solvent	α (Kamlet-Taft)	β (Kamlet-Taft)	E_T (Dimroth-Reichardt)	# of hydrogen bond donors	# of hydrogen bond acceptors
CH_3CN	0.19	0.40	45.6	0	1
$C_4H_6O_2$	0	0.49	44.3	0	4
CH_3OH	0.98	0.66	55.4	1	2
H_2O	1.17	0.47	63.1	2	2

Table S5. Hydrogen bonding donating ability (α), hydrogen bond accepting ability (β), Dimroth-Reichardt parameter (E_T), and the number of hydrogen bond donors and acceptors for each solvent used in the study. The Kamlet-Taft and Reichardt parameters are previously tabulated values.[33]
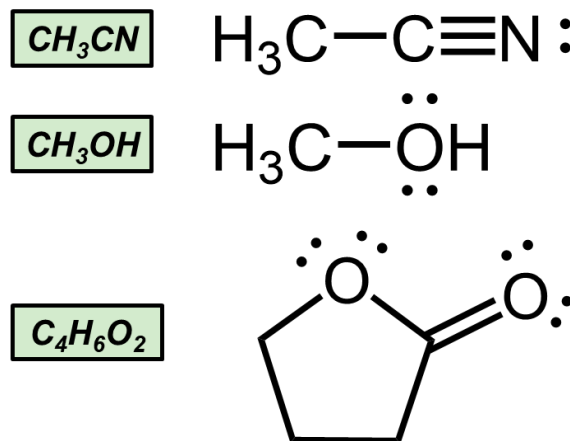
Scheme S1. Structures of the organic solvents used in the study.

The Kamlet-Taft and Dimroth-Reichardt parameters are determined from the energies of the longest wavelength absorption peaks of probe solutes into each solvent. The Kamlet-Taft parameters, number of hydrogen bond donors and acceptors (see Scheme S1 for illustration), and excess enthalpies of mixing (Figure S20) provide measures of the strength of interactions between the three organic solvents and H_2O. The Dimroth-Reichardt parameter provides a measure of the ionizing power of a solvent.[34]

Overall, the information from Table S5, Scheme S1, and Figure S20 provides evidence that among the organic solvents in this study, H_2O hydrogen bonds most strongly with CH_3OH and least strongly with CH_3CN.
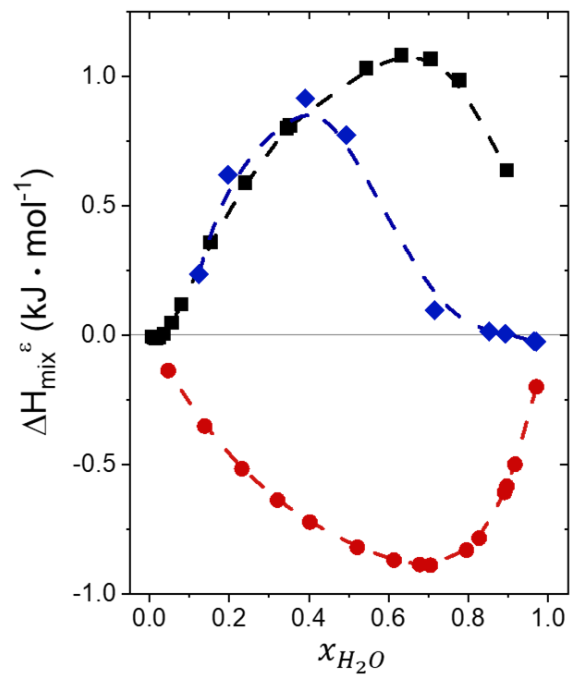
Figure S20. Excess enthalpy of mixing ($\Delta H_{mix}^{\varepsilon}$) as a function of x_{H_2O} in mixtures of CH_3OH (●), b) CH_3CN (■), and c) $C_4H_6O_2$ (◆) with H_2O, obtained from previous reports.[35-37]

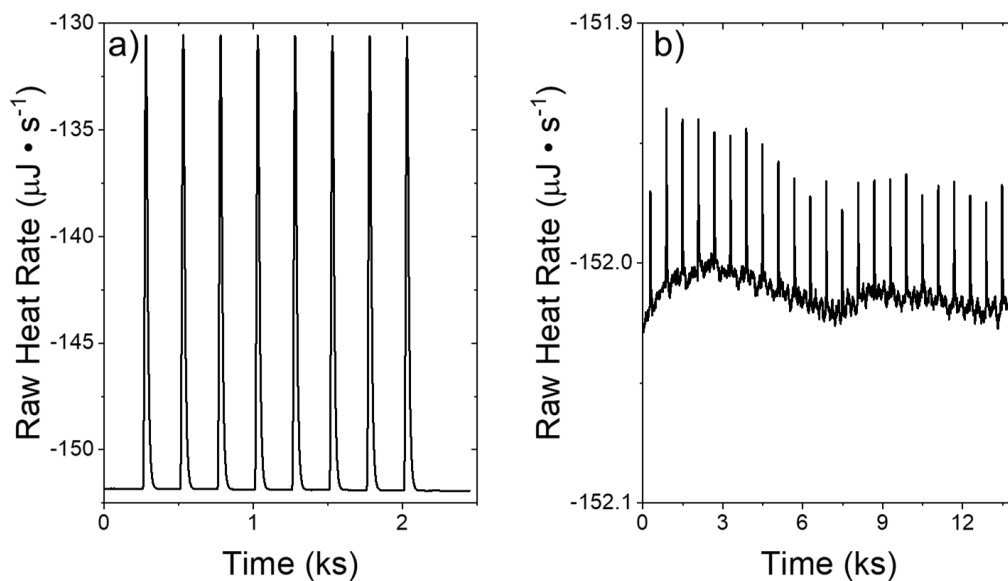## S11. Isothermal Titration Calorimetry Thermograms and Heats per Epoxide Injection

Figure S21. a) ITC thermogram from the electrical calibration of the NanoITC. b) ITC thermogram from the water-water adsorption to check the cleanliness of the ITC cell.

The plots in Figure S21 were obtained during the cleaning and calibration procedures for isothermal titration calorimetry (ITC), as discussed in Section 2.5 of the main text. Figure S21a shows the heat released from the sequential pulses during the electrical calibration. The instrument gave a calibration factor after completion, for which values greater than 0.98 were assumed to be satisfactory. Figure S21b shows the heat released during the water-water injection, during which each 1 μL injection led to a peak with an area between -3 and +3 μJ.
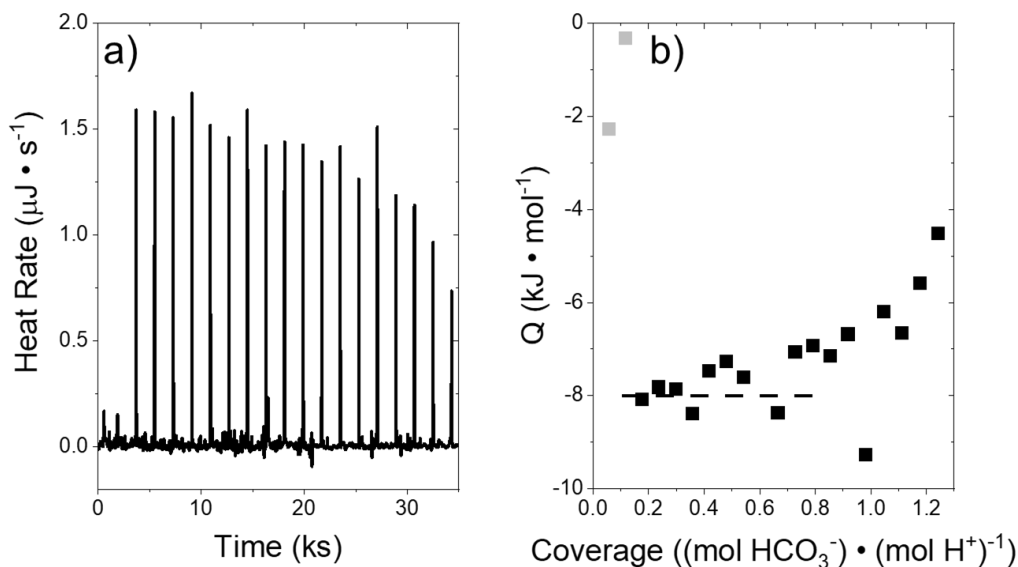
Figure S22. a) ITC thermogram from the acid-base titration of HNO_3 (0.0005 M in 0.1 M NaCl) with $NaHCO_3$ (0.0052 M in 0.1 M NaCl), b) the corresponding heats released as a function of bicarbonate ion coverage.

Figure S22 shows an acid-base titration of $NaHCO_3$ into HNO_3, which was used as a standard to verify the results obtained from the NanoITC. The adsorption enthalpy calculated from Figure S22b was -8.1 ± 1.2 kJ mol^{-1}. This measurement agrees well with the reported enthalpy of -9.1 kJ mol^{-1}.[38-39]

The ITC thermogram and heat release plots for all ITC experiments (other than that in Figure 8 in the main text) are shown below. As discussed in Section 3.6, early injections often show lower heat released than expected due to the evaporation of liquid from the syringe needle. Although less common, some of the experiments below show outlier points at later injections, which may result from an inconsistent volume or epoxide concentration in those injections.
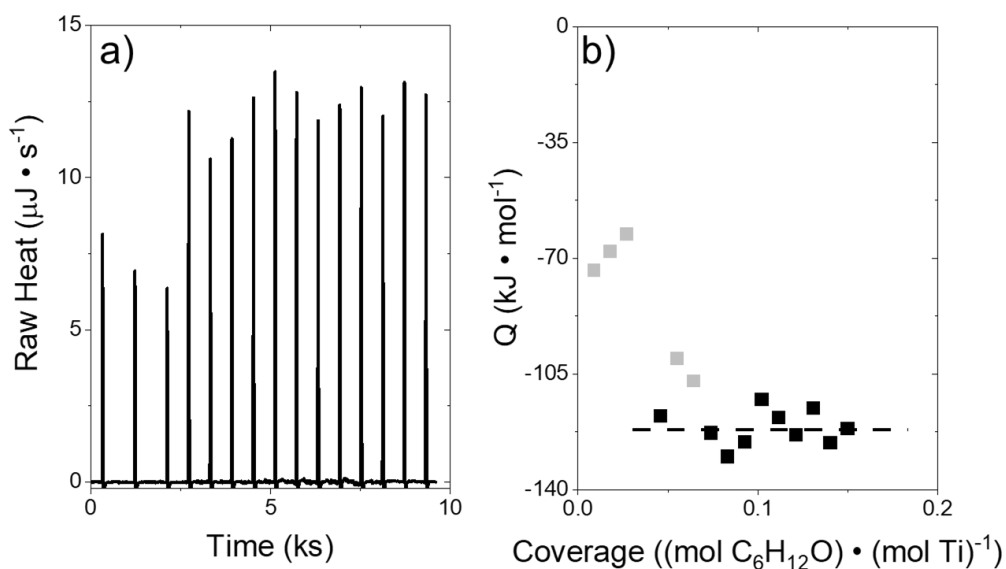
Figure S23. a) ITC thermogram from the titration of Ti-BEA-OH with 1,2-epoxyhexane (5 mM $C_6H_{12}O$ in CH_3CN with 39 mM H_2O ($x_{H_2O} = 0.002$), 313 K, 1 μL per injection), b) the corresponding heats released as a function of 1,2-epoxyhexane coverage.
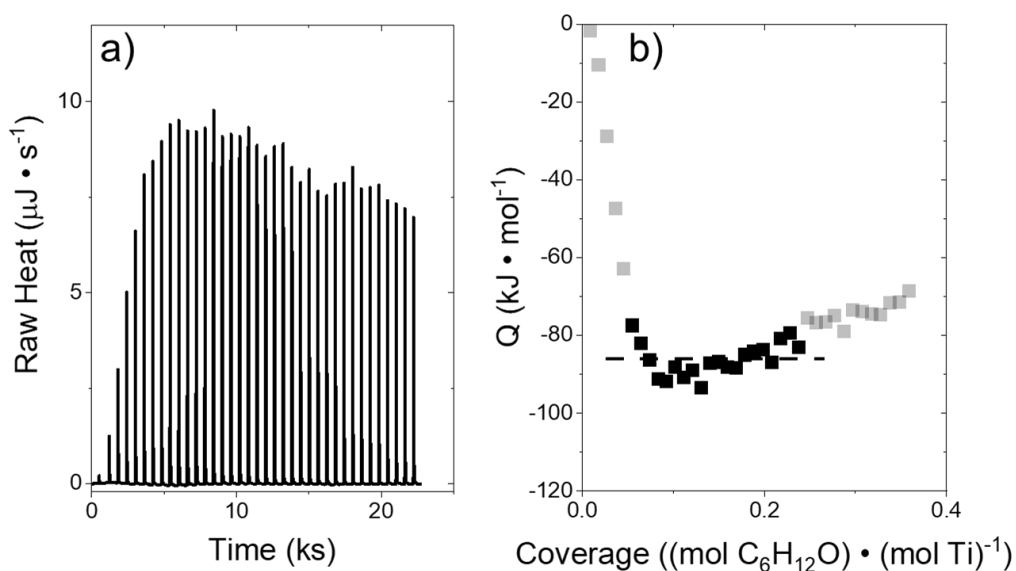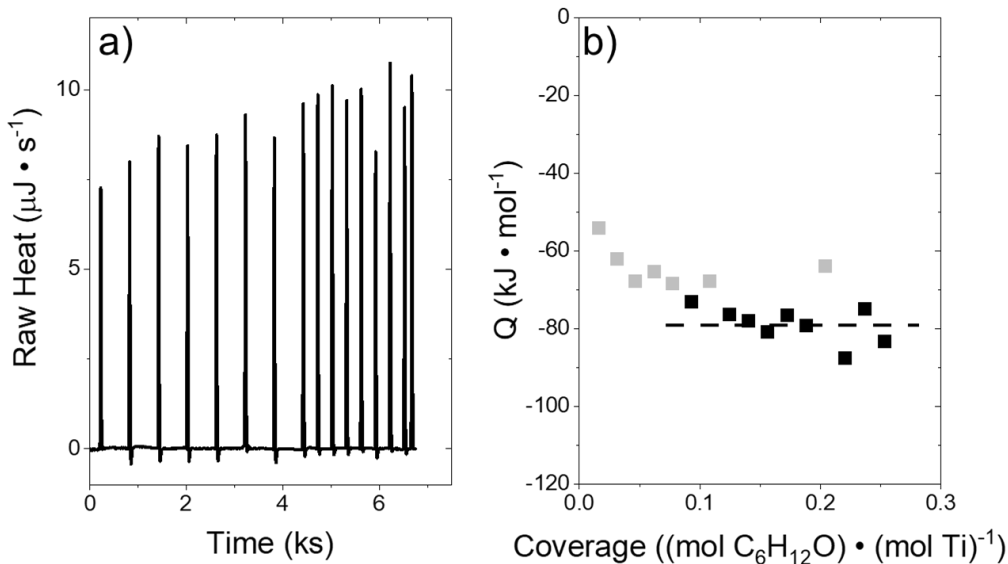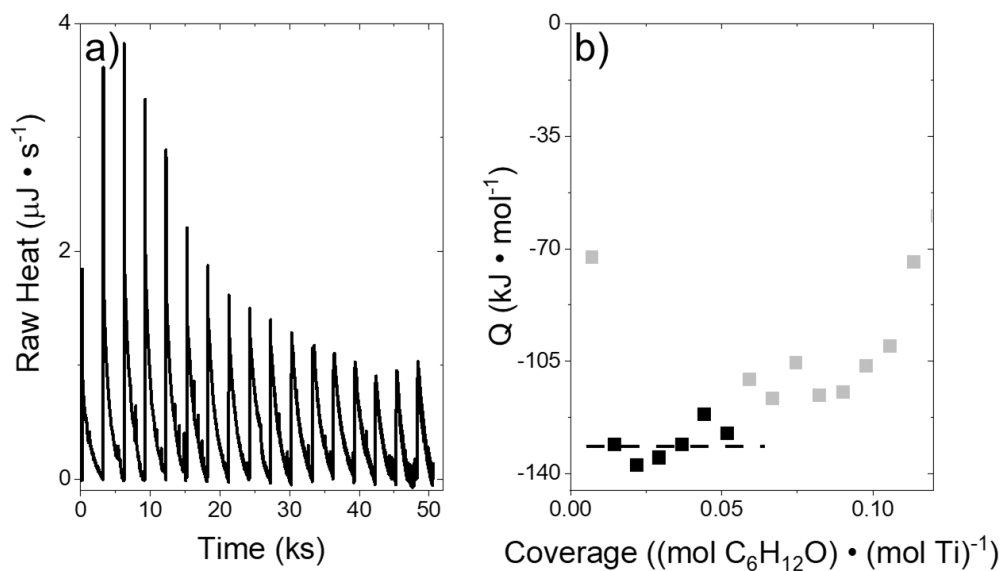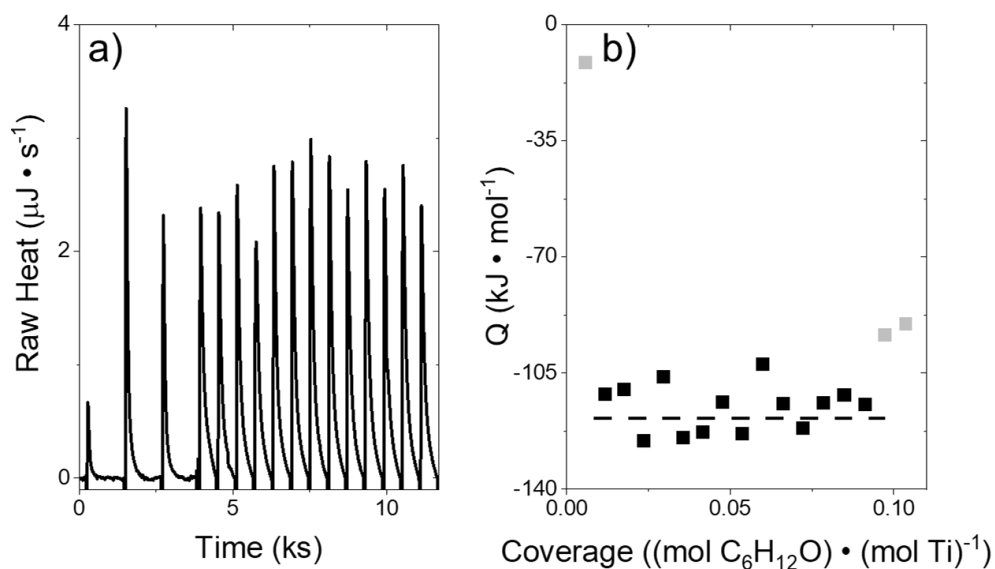

Figure S24. a) ITC thermogram from the titration of Ti-BEA-OH with 1,2-epoxyhexane (5 mM $C_6H_{12}O$ in $x_{CH_3CN} = 0.9$ (18.4 M) with H_2O (2.1 M), 313 K, 1 μL per injection), b) the corresponding heats released as a function of 1,2-epoxyhexane coverage.
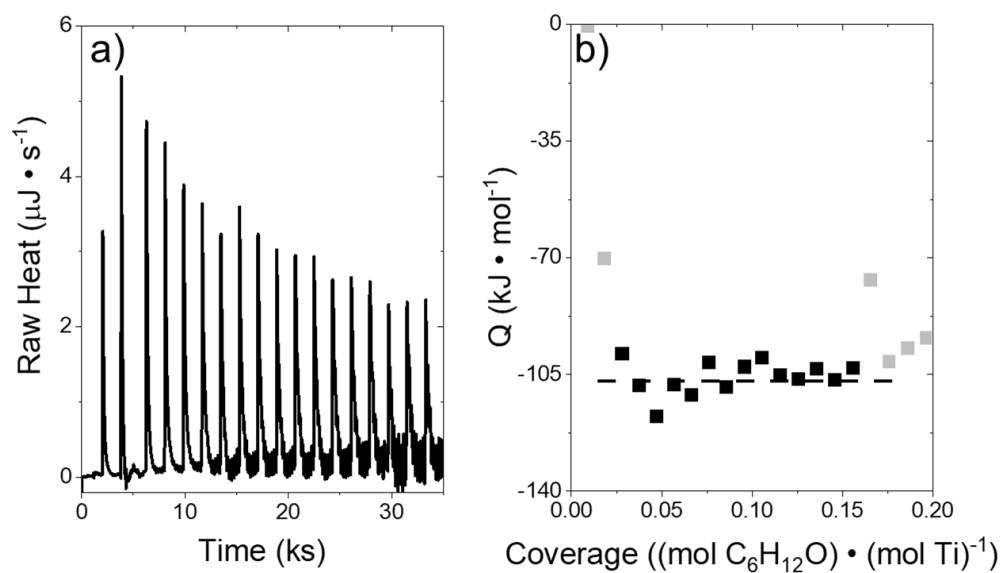
Figure S25. a) ITC thermogram from the titration of Ti-BEA-OH with 1,2-epoxyhexane (5 mM $C_6H_{12}O$ in $x_{CH_3CN} = 0.35$ (11.7 M) with H_2O (21.6 M), 313 K, 1 µL per injection), b) the corresponding heats released as a function of 1,2-epoxyhexane coverage.

Figure S26. a) ITC thermogram from the titration of Ti-BEA-F with 1,2-epoxyhexane (5 mM $C_6H_{12}O$ in CH_3CN with 39 mM H_2O ($x_{H_2O} = 0.002$), 313 K, 1 µL per injection), b) the corresponding heats released as a function of 1,2-epoxyhexane coverage.

Figure S27. a) ITC thermogram from the titration of Ti-BEA-F with 1,2-epoxyhexane (5 mM $C_6H_{12}O$ in $x_{CH_3CN} = 0.9$ (18.4 M) with H_2O (2.1 M), 313 K, 1 μL per injection), b) the corresponding heats released as a function of 1,2-epoxyhexane coverage.
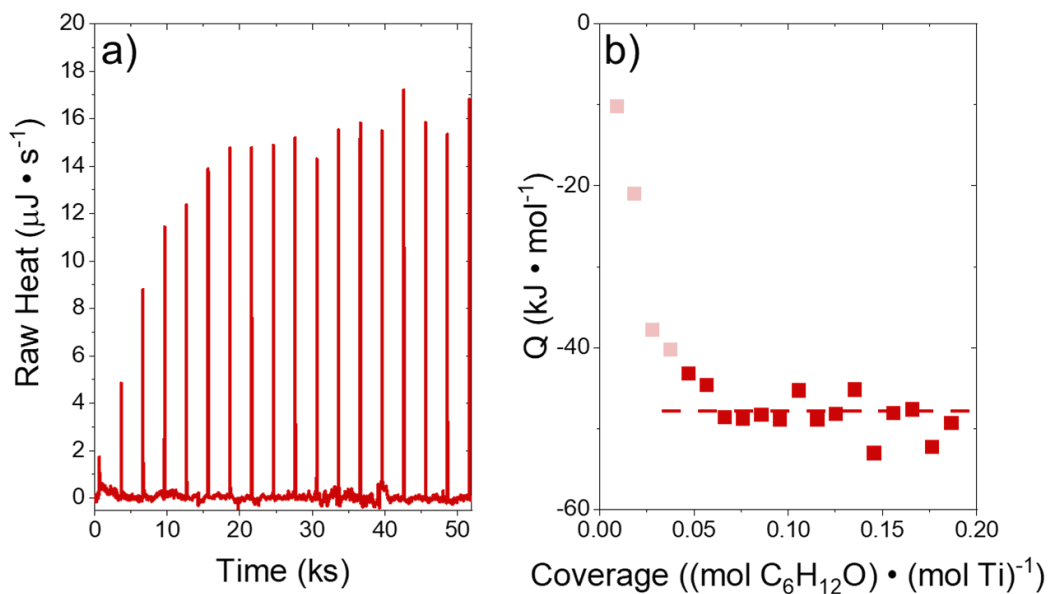

Figure S28. a) ITC thermogram from the titration of Ti-BEA-F with 1,2-epoxyhexane (5 mM $C_6H_{12}O$ in $x_{CH_3CN} = 0.35$ (11.7 M) with H_2O (21.6 M), 313 K, 1 μL per injection), b) the corresponding heats released as a function of 1,2-epoxyhexane coverage.

Figure S29. a) ITC thermogram from the titration of Ti-BEA-OH with 1,2-epoxyhexane (10 mM $C_6H_{12}O$ in CH_3OH with 39 mM H_2O (x_{H_2O} = 0.002), 313 K, 1 μL per injection), b) the corresponding heats released as a function of 1,2-epoxyhexane coverage.
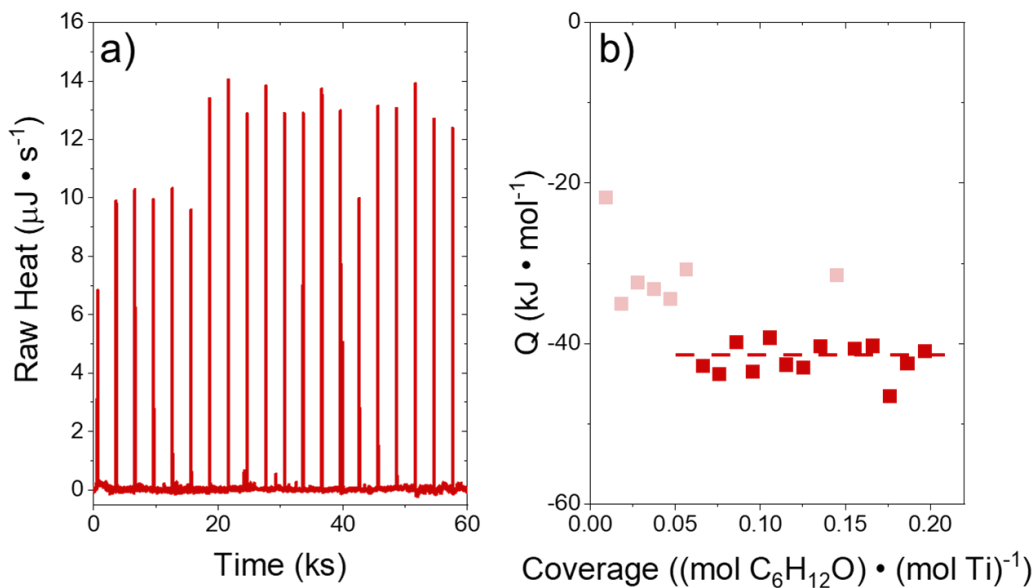

Figure S30. a) ITC thermogram from the titration of Ti-BEA-OH with 1,2-epoxyhexane (10 mM $C_6H_{12}O$ in x_{CH_3OH} = 0.8 (22.2 M) with H_2O (5.6 M), 313 K, 1 μL per injection), b) the corresponding heats released as a function of 1,2-epoxyhexane coverage.
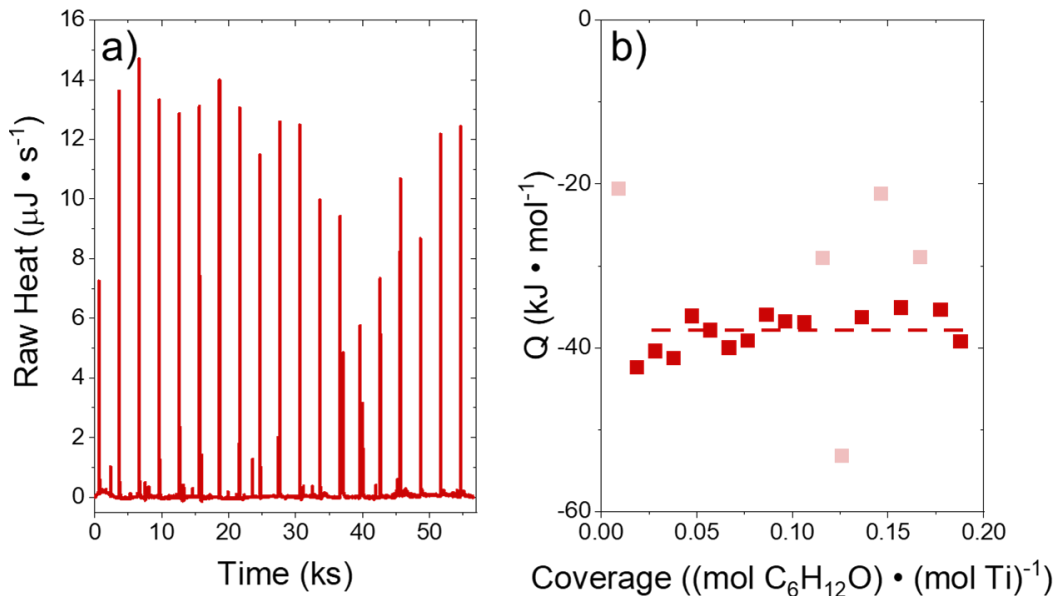
Figure S31. a) ITC thermogram from the titration of Ti-BEA-OH with 1,2-epoxyhexane (10 mM $C_6H_{12}O$ in x_{CH_3OH} = 0.5 (17.1 M) with H_2O (17.1 M), 313 K, 1 μL per injection), b) the corresponding heats released as a function of 1,2-epoxyhexane coverage.
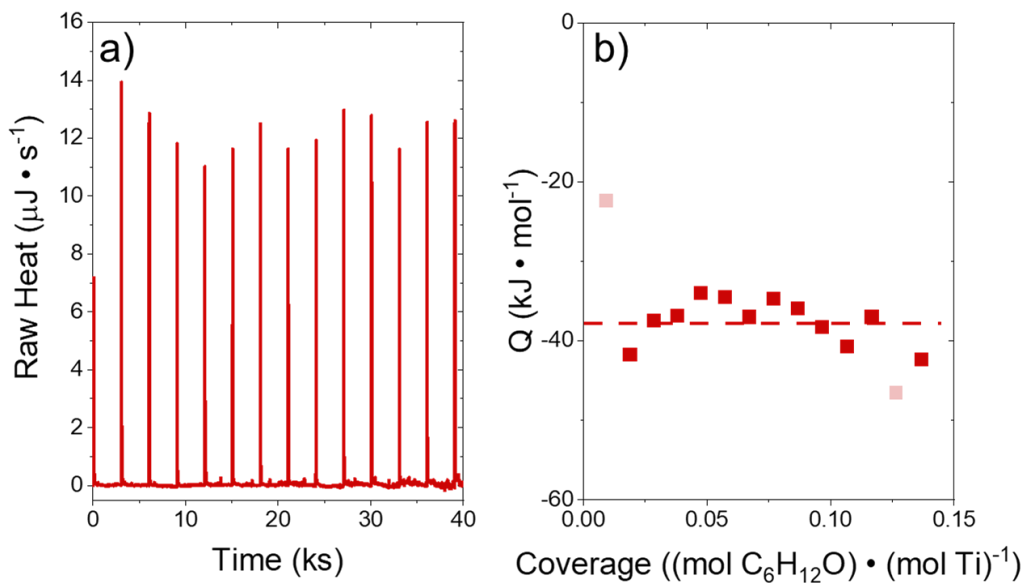

Figure S32. a) ITC thermogram from the titration of Ti-BEA-OH with 1,2-epoxyhexane (10 mM $C_6H_{12}O$ in x_{CH_3OH} = 0.3 (12.1 M) with H_2O (28.3 M), 313 K, 1 μL per injection), b) the corresponding heats released as a function of 1,2-epoxyhexane coverage.
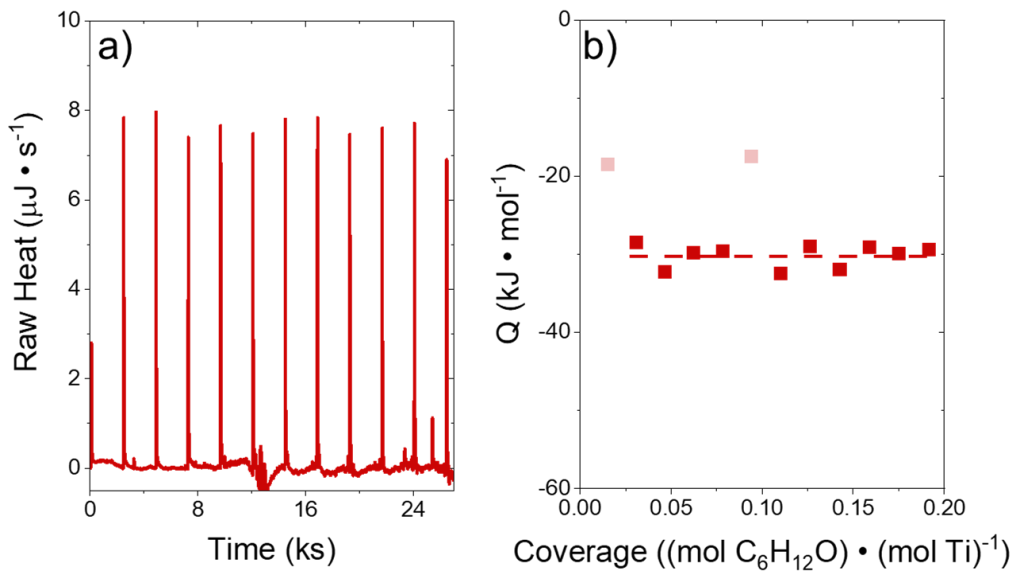
Figure S33. a) ITC thermogram from the titration of Ti-BEA-F with 1,2-epoxyhexane (10 mM $C_6H_{12}O$ in CH_3OH with 39 mM H_2O ($x_{H_2O} = 0.002$), 313 K, 1 μL per injection), b) the corresponding heats released as a function of 1,2-epoxyhexane coverage.
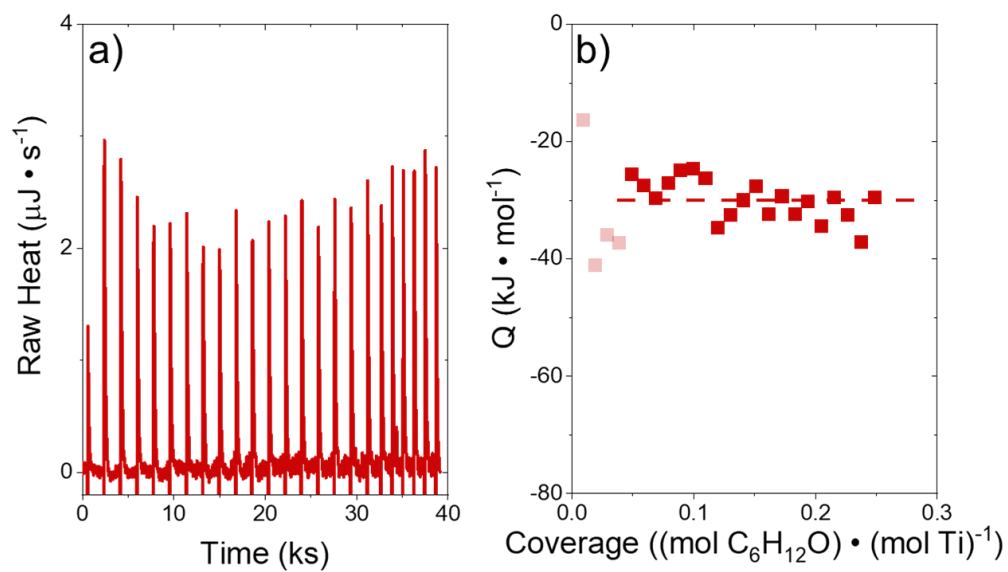

Figure S34. a) ITC thermogram from the titration of Ti-BEA-F with 1,2-epoxyhexane (10 mM $C_6H_{12}O$ in $x_{CH_3OH} = 0.5$ (17.1 M) with H_2O (17.1 M), 313 K, 1 μL per injection), b) the corresponding heats released as a function of 1,2-epoxyhexane coverage.
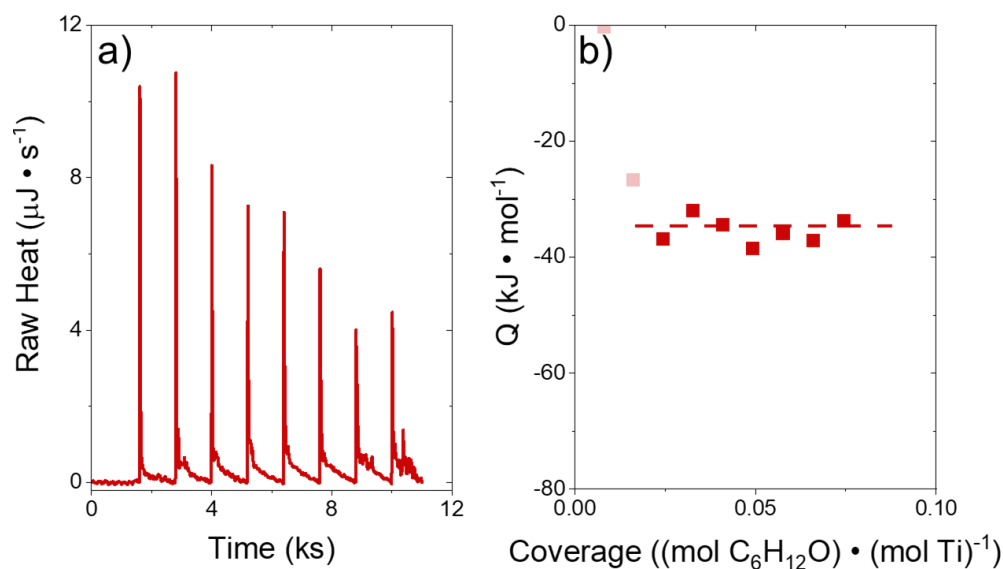
Figure S35. a) ITC thermogram from the titration of Ti-BEA-F with 1,2-epoxyhexane (10 mM $C_6H_{12}O$ in $x_{CH_3OH} =$ 0.3 (12.1 M) with H_2O (28.3 M), 313 K, 1 μL per injection), b) the corresponding heats released as a function of 1,2-epoxyhexane coverage.

Figure S36. a) ITC thermogram from the titration of Ti-BEA-OH with 1,2-epoxyhexane (10 mM $C_6H_{12}O$ in $C_4H_6O_2$ with 39 mM H_2O ($x_{H_2O} = 0.002$), 313 K, 1 μL per injection), b) the corresponding heats released as a function of 1,2-epoxyhexane coverage.
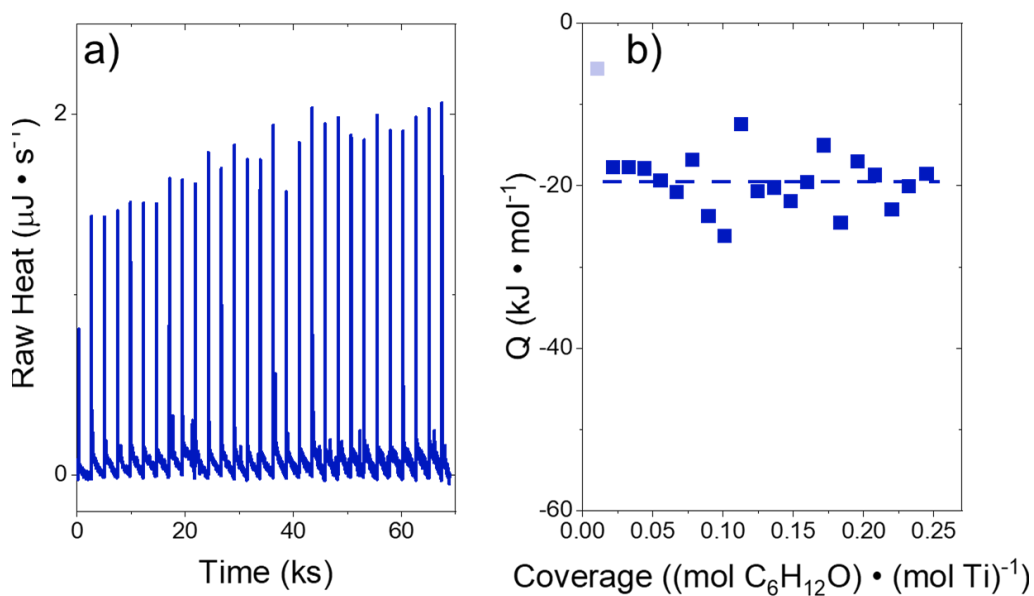
Figure S37. a) ITC thermogram from the titration of Ti-BEA-F with 1,2-epoxyhexane (10 mM $C_6H_{12}O$ in $C_4H_6O_2$ with 39 mM H_2O (x_{H_2O} = 0.002), 313 K, 1 μL per injection), b) the corresponding heats released as a function of 1,2-epoxyhexane coverage.
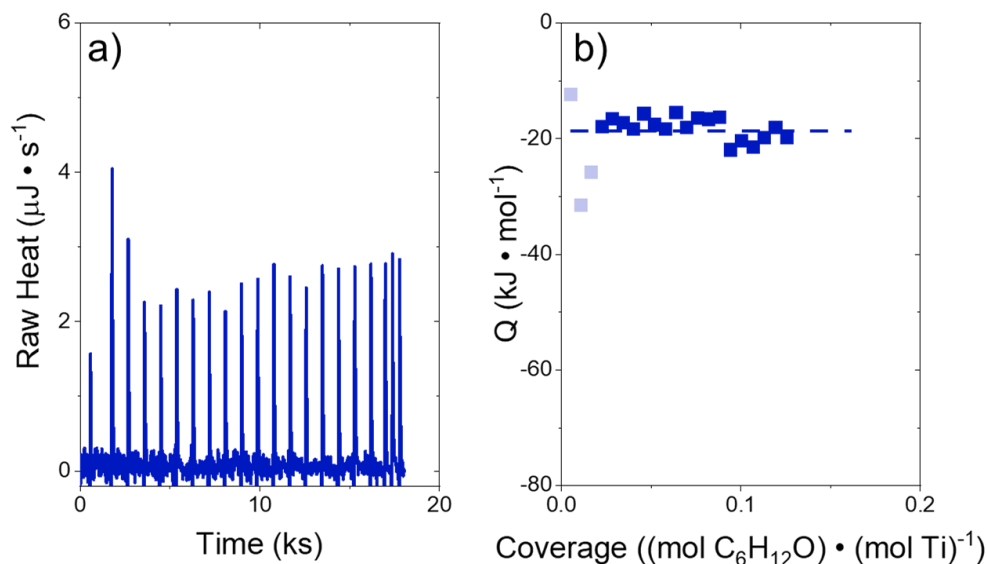

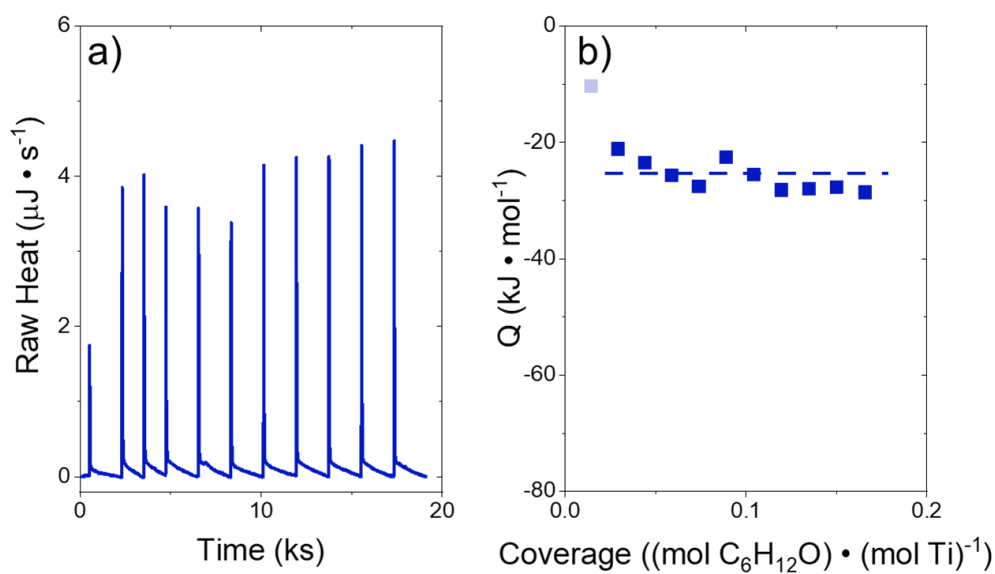**Figure S38.** a) ITC thermogram from the titration of Ti-BEA-F with 1,2-epoxyhexane (10 mM $C_6H_{12}O$ in $x_{C_4H_6O_2}$ = 0.8 (12.4 M) with H_2O (3.1 M), 313 K, 1 μL per injection), b) the corresponding heats released as a function of 1,2-epoxyhexane coverage.
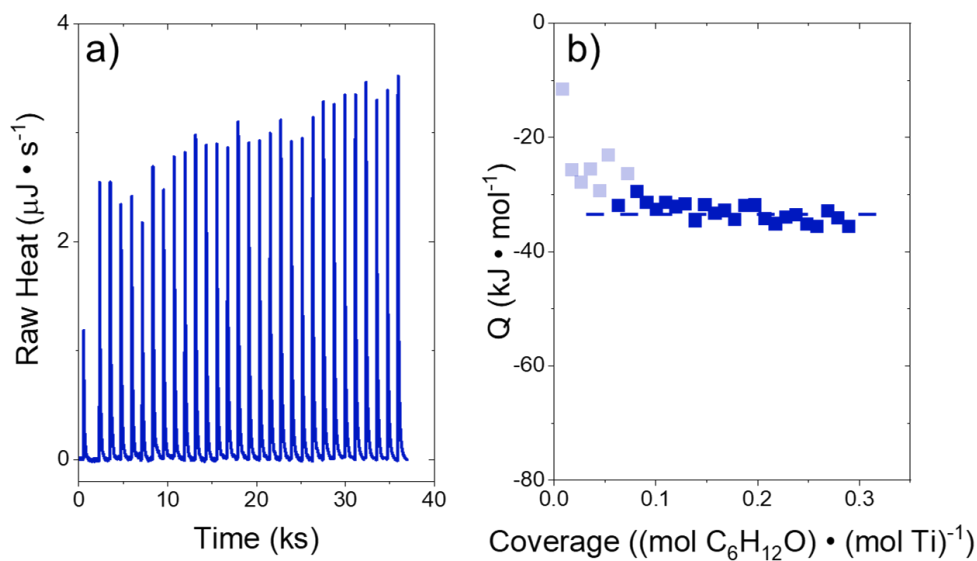
Figure S39. a) ITC thermogram from the titration of Ti-BEA-OH with 1,2-epoxyhexane (10 mM $C_6H_{12}O$ in $x_{C_4H_6O_2}$ = 0.8 (12.4 M) with H_2O (3.1 M), 313 K, 1 μL per injection), b) the corresponding heats released as a function of 1,2-epoxyhexane coverage.

Figure S40. a) ITC thermogram from the titration of Ti-BEA-F with 1,2-epoxyhexane (5 mM $C_6H_{12}O$ in $x_{C_4H_6O_2}$ = 0.25 (7.6 M) with H_2O (22.8 M), 313 K, 1 μL per injection), b) the corresponding heats released as a function of 1,2-epoxyhexane coverage.
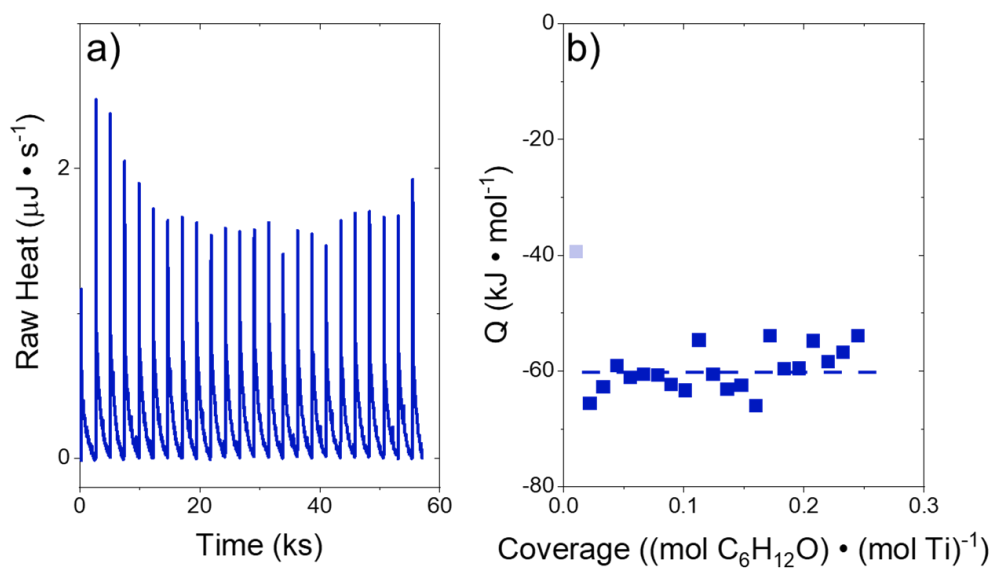
References

1. Dette, C.; Pérez-Osorio, M. A.; Kley, C. S.; Punke, P.; Patrick, C. E.; Jacobson, P.; Giustino, F.; Jung, S. J.; Kern, K., TiO2 Anatase with a Bandgap in the Visible Region. *Nano Letters* **2014,** *14* (11), 6533-6538.
2. Camblor, M. A.; Corma, A.; Valencia, S., Synthesis in fluoride media and characterisation of aluminosilicate zeolite beta. *Journal of Materials Chemistry* **1998,** *8* (9), 2137-2145.
3. Vega-Vila, J. C.; Harris, J. W.; Gounder, R., Controlled insertion of tin atoms into zeolite framework vacancies and consequences for glucose isomerization catalysis. *J Catal* **2016,** *344*, 108-120.
4. Shirke, B. S.; Korake, P. V.; Hankare, P. P.; Bamane, S. R.; Garadkar, K. M., Synthesis and characterization of pure anatase TiO2 nanoparticles. *Journal of Materials Science: Materials in Electronics* **2011,** *22* (7), 821-824.
5. Ohsaka, T.; Izumi, F.; Fujiki, Y., Raman spectrum of anatase, TiO2. *Journal of Raman Spectroscopy* **1978,** *7* (6), 321-324.
6. Signorile, M.; Crocellà, V.; Damin, A.; Rossi, B.; Lamberti, C.; Bonino, F.; Bordiga, S., Effect of Ti Speciation on Catalytic Performance of TS-1 in the Hydrogen Peroxide to Propylene Oxide Reaction. *The Journal of Physical Chemistry C* **2018,** *122* (16), 9021-9034.
7. Mihailova, B.; Valtchev, V.; Mintova, S.; Faust, A. C.; Petkov, N.; Bein, T., Interlayer stacking disorder in zeolite beta family: a Raman spectroscopic study. *Physical Chemistry Chemical Physics* **2005,** *7* (14), 2756.
8. Tosheva, L.; Mihailova, B.; Valtchev, V.; Sterte, J., Zeolite beta spheres. *Microporous and Mesoporous Materials* **2001,** *48* (1-3), 31-37.
9. Majano, G.; Mintova, S.; Ovsitser, O.; Mihailova, B.; Bein, T., Zeolite Beta nanosized assemblies. *Microporous and Mesoporous Materials* **2005,** *80* (1-3), 227-235.
10. Inagaki, S.; Nakatsuyama, K.; Saka, Y.; Kikuchi, E.; Kohara, S.; Matsukata, M., Elucidation of Medium-Range Structure in a Dry Gel-Forming *BEA-Type Zeolite. *The Journal of Physical Chemistry C* **2007,** *111* (28), 10285-10293.
11. Yu, Y.; Xiong, G.; Li, C.; Xiao, F.-S., Characterization of aluminosilicate zeolites by UV Raman spectroscopy. *Microporous and Mesoporous Materials* **2001,** *46* (1), 23-34.
12. Knops-Gerrits, P.-P.; De Vos, D. E.; Feijen, E. J.; Jacobs, P. A., Raman spectroscopy on zeolites. *Microporous Materials* **1997,** *8* (1-2), 3-17.
13. Scarano, D.; Zecchina, A.; Bordiga, S.; Geobaldo, F.; Spoto, G.; Petrini, G.; Leofanti, G.; Padovan, M.; Tozzola, G., Fourier-transform infrared and Raman spectra of pure and Al-, B-, Ti- and Fe-substituted silicalites: stretching-mode region. *Journal of the Chemical Society, Faraday Transactions* **1993,** *89* (22), 4123.
14. Blasco, T.; Camblor, M. A.; Corma, A.; Esteve, P.; Guil, J. M.; Martinez, A.; Perdigon-Melon, J. A.; Valencia, S., Direct synthesis and characterization of hydrophobic aluminum-free Ti-beta zeolite. *Journal of Physical Chemistry B* **1998,** *102*, 75-88.
15. Mihailova, B.; Valtchev, V.; Mintova, S.; Faust, A.-C.; Petkov, N.; Bein, T., Interlayer stacking disorder in zeolite beta family: a Raman spectroscopic study. *Physical chemistry chemical physics* **2005,** *7* (14), 2756-2763.
16. Bordiga, S.; Damin, A.; Bonino, F.; Zecchina, A.; Spanò, G.; Rivetti, F.; Bolis, V.; Prestipino, C.; Lamberti, C., Effect of Interaction with H2O and NH3 on the Vibrational, Electronic, and Energetic Peculiarities of Ti(IV) Centers TS-1 Catalysts: A Spectroscopic and Computational Study. *The Journal of Physical Chemistry B* **2002,** *106* (38), 9892-9905.
17. Dartt, C. B.; Davis, M. E., Characterization and catalytic activity of titanium containing SSZ-33 and aluminum-free zeolite beta. *Applied Catalysis A: General* **1996,** *143* (1), 53-73.
18. Bordiga, S.; Damin, A.; Bonino, F.; Ricchiardi, G.; Zecchina, A.; Tagliapietra, R.; Lamberti, C., Resonance Raman effects in TS-1: the structure of Ti(iv) species and reactivity towards H2O, NH3 and H2O2: an in situ studyPresented at the International Congress on Operando Spectroscopy, Lunteren, The Netherlands, March 2-6, 2003. *Physical Chemistry Chemical Physics* **2003,** *5* (20), 4390.

19. Ricchiardi, G.; Damin, A.; Bordiga, S.; Lamberti, C.; Spanò, G.; Rivetti, F.; Zecchina, A., Vibrational Structure of Titanium Silicate Catalysts. A Spectroscopic and Theoretical Study. *Journal of the American Chemical Society* **2001,** *123* (46), 11409-11419.

20. Li, C.; Xiong, G.; Liu, J.; Ying, P.; Xin, Q.; Feng, Z., Identifying Framework Titanium in TS-1 Zeolite by UV Resonance Raman Spectroscopy. *The Journal of Physical Chemistry B* **2001,** *105* (15), 2993-2997.

21. Bregante, D. T.; Tan, J. Z.; Schultz, R. L.; Ayla, E. Z.; Potts, D. S.; Torres, C.; Flaherty, D. W., Catalytic Consequences of Oxidant, Alkene, and Pore Structures on Alkene Epoxidations within Titanium Silicates. *ACS Catalysis* **2020,** *10* (17), 10169-10184.

22. Tang, B.; Dai, W.; Wu, G.; Guan, N.; Li, L.; Hunger, M., Improved Postsynthesis Strategy to Sn-Beta Zeolites as Lewis Acid Catalysts for the Ring-Opening Hydration of Epoxides. *ACS Catalysis* **2014,** *4* (8), 2801-2810.

23. Ardagh, M. A.; Bregante, D. T.; Flaherty, D. W.; Notestein, J. M., Controlled Deposition of Silica on Titania-Silica to Alter the Active Site Surroundings on Epoxidation Catalysts. *ACS Catalysis* **2020,** *10* (21), 13008-13018.

24. Tan, J. Z.; Bregante, D. T.; Torres, C.; Flaherty, D. W., Transition state stabilization depends on solvent identity, pore size, and hydrophilicity for epoxidations in zeolites. *J Catal* **2022,** *405*, 91-104.

25. Vega-Vila, J. C.; Gounder, R., Quantification of Intraporous Hydrophilic Binding Sites in Lewis Acid Zeolites and Consequences for Sugar Isomerization Catalysis. *ACS Catalysis* **2020,** *10* (20), 12197-12211.

26. Cordon, M. J.; Harris, J. W.; Vega-Vila, J. C.; Bates, J. S.; Kaur, S.; Gupta, M.; Witzke, M. E.; Wegener, E. C.; Miller, J. T.; Flaherty, D. W.; Hibbitts, D. D.; Gounder, R., Dominant Role of Entropy in Stabilizing Sugar Isomerization Transition States within Hydrophobic Zeolite Pores. *Journal of the American Chemical Society* **2018,** *140* (43), 14244-14266.

27. Di Iorio, J. R.; Johnson, B. A.; Román-Leshkov, Y., Ordered Hydrogen-Bonded Alcohol Networks Confined in Lewis Acid Zeolites Accelerate Transfer Hydrogenation Turnover Rates. *Journal of the American Chemical Society* **2020,** *142* (45), 19379-19392.

28. Bregante, D. T.; Flaherty, D. W., Periodic Trends in Olefin Epoxidation over Group IV and V Framework-Substituted Zeolite Catalysts: A Kinetic and Spectroscopic Study. *Journal of the American Chemical Society* **2017,** *139* (20), 6888-6898.

29. Ayla, E. Z.; Potts, D. S.; Bregante, D. T.; Flaherty, D. W., Alkene Epoxidations with H2O2 over Groups 4–6 Metal-Substituted BEA Zeolites: Reactive Intermediates, Reaction Pathways, and Linear Free-Energy Relationships. *ACS Catalysis* **2021,** *11* (1), 139-154.

30. Bregante, D. T.; Thornburg, N. E.; Notestein, J. M.; Flaherty, D. W., Consequences of Confinement for Alkene Epoxidation with Hydrogen Peroxide on Highly Dispersed Group 4 and 5 Metal Oxide Catalysts. *ACS Catalysis* **2018,** *8* (4), 2995-3010.

31. Eyring, H., The Activated Complex and the Absolute Rate of Chemical Reactions. *Chemical Reviews* **1935,** *17* (1), 65-77.

32. Madon, R. J.; Iglesia, E., Catalytic reaction rates in thermodynamically non-ideal systems. *Journal of Molecular Catalysis A: Chemical* **2000,** *163* (1-2), 189-204.

33. Marcus, Y., The properties of organic liquids that are relevant to their use as solvating solvents. *Chemical Society Reviews* **1993,** *22* (6), 409-416.

34. Reichardt, C.; Dimroth, K., Lösungsmittel und empirische Parameter zur Charakterisierung ihrer Polarität. In *Lösungen und Lösungsmittel*, Springer: 1968; pp 1-73.

35. Ramkumar, D.; Kudchadker, A.; Deshpande, D., Enthalpies of mixing of tetrahydrofuran+. gamma.-butyrolactone and water+. gamma.-butyrolactone systems at 299.15 K. *Journal of Chemical and Engineering Data* **1985,** *30* (4), 491-492.

36. Morcom, K.; Smith, R., Enthalpies of mixing of water+ methyl cyanide. *The Journal of Chemical Thermodynamics* **1969,** *1* (5), 503-505.

37. Benjamin, L.; Benson, G., A DEUTERIUM ISOTOPE EFFECT ON THE EXCESS ENTHALPY OF METHANOL—WATER SOLUTIONS1. *The Journal of physical chemistry* **1963,** *67* (4), 858-861.

38. Goldberg, R. N.; Kishore, N.; Lennen, R. M., Thermodynamic Quantities for the Ionization Reactions of Buffers. *Journal of Physical and Chemical Reference Data* **2002,** *31* (2), 231-370.

39. Berg, R. L.; Vanderzee, C. E., Enthalpies of dilution of sodium carbonate and sodium hydrogen carbonate solutions, and the standard enthalpies of ionization of aqueous carbonic acid, at 298.15 K. *The Journal of Chemical Thermodynamics* **1978,** *10* (11), 1049-1075.